ARMY RESEARCH LABORATORY

Computational Overlap Coupling Between Micropolar Linear Elastic Continuum Finite Elements and Nonlinear Elastic Spherical Discrete Elements in One Dimension

by Richard A. Regueiro
Associate Professor
Department of Civil, Environmental, and Architectural Engineering
University of Colorado at Boulder
1111 Engineering Dr.
428 UCB, ECOT 441
Boulder, CO 80309-0428

ARL-CR-0710 **January 2013**

NOTICES

Disclaimers

The findings in this report are not to be construed as an official Department of the Army position unless so designated by other authorized documents.

Citation of manufacturer’s or trade names does not constitute an official endorsement or approval of the use thereof.

Destroy this report when it is no longer needed. Do not return it to the originator.

Army Research Laboratory

Aberdeen Proving Ground, MD 21005-5066

ARL-CR-0710 **January 2013**

Computational Overlap Coupling Between Micropolar Linear Elastic Continuum Finite Elements and Nonlinear Elastic Spherical Discrete Elements in One Dimension

Richard A. Regueiro

Department of Civil, Environmental, and Architectural Engineering

University of Colorado at Boulder

1111 Engineering Dr.

428 UCB, ECOT 441

Boulder, CO 80309-0428

REPORT DOCUMENTATION PAGE	Form Approved OMB No. 0704-0188

1. REPORT DATE *(DD-MM-YYYY)*	2. REPORT TYPE	3. DATES COVERED (From - To)
January 2013	Final	1 Jun 2010 - 1 June 2011

4. TITLE AND SUBTITLE
Computational Overlap Coupling Between Micropolar Linear Elastic Continuum Finite Elements and Nonlinear Elastic Spherical Discrete Elements in One Dimension

5a. CONTRACT NUMBER
W911NF-07-D-0001

5b. GRANT NUMBER

5c. PROGRAM ELEMENT NUMBER

6. AUTHOR(S)
Richard A. Regueiro

5d. PROJECT NUMBER

5e. TASK NUMBER

5f. WORK UNIT NUMBER

7. PERFORMING ORGANIZATION NAME(S) AND ADDRESS(ES)
University of Colorado at Boulder
1111 Engineering Dr.
Boulder, CO 80309

8. PERFORMING ORGANIZATION REPORT NUMBER
ARL-CR-0710

9. SPONSORING/MONITORING AGENCY NAME(S) AND ADDRESS(ES)
U.S. Army Research Office
P.O. Box 12211
Research Triangle Park, NC 27709

10. SPONSOR/MONITOR'S ACRONYM(S)
ARO

11. SPONSOR/MONITOR'S REPORT NUMBER(S)
TCN 10-077

12. DISTRIBUTION/AVAILABILITY STATEMENT
Approved for public release; distribution is unlimited.

13. SUPPLEMENTARY NOTES
Task was performed under a Scientific Services Agreement issued by Battelle Chapel Hill Operations, 50101 Governors Drive, Suite 110, Chapel Hill, NC 27517

14. ABSTRACT
The report presents a one dimensional (1D) problem for overlap coupling between a micropolar linear elastic 1D mixed finite element (FE) model and a 1D string of Hertzian nonlinear elastic discrete element spheres. The 1D micropolar balance equations and linear elastic constitutive equations are derived from the three-dimensional (3D) theory by assuming Timoshenko beam kinematics with axial stretch. They are formulated in weak form, where upon introducing interpolation functions, lead to coupled, linear 1D micropolar FE matrix equations. The nonlinear vector equations for a string of Hertzian nonlinear elastic, glued, discrete element (DE) spheres are derived and solved by the Newton-Raphson method. The 1D micropolar FEs and 1D string of DEs are coupled using a bridging-scale decomposition as a point of departure. 1D numerical examples for full overlap coupling, and partial overlap coupling, for quasi-statics are demonstrated. The formulation is general for quasi-statics and dynamics.

15. SUBJECT TERMS
finite element/discrete element coupling; micropolar linear elasticity; Timoshenko beam kinematics; small strain

16. SECURITY CLASSIFICATION OF:			17. LIMITATION OF ABSTRACT	18. NUMBER OF PAGES	19a. NAME OF RESPONSIBLE PERSON
a. REPORT	b. ABSTRACT	c. THIS PAGE			John Clayton
Unclassified	Unclassified	Unclassified	UU	58	19b. TELEPHONE NUMBER (*Include area code*) 410-278-6146

Contents

List of Figures

Acknowledgment

This work was supported by the ‘RDECOM-ARL: Army Research Laboratory’ (Dr. John Clayton) under the auspices of the U.S. Army Research Office Scientific Services Program administered by Battelle (Delivery Order 0921, Contract No. W911NF-07-D-0001).

INTENTIONALLY LEFT BLANK.

1. Introduction

1.1 Description of Problem

Dynamic failure in bound particulate materials is a combination of physical processes including grain and matrix deformation, intra-granular cracking, matrix cracking, and inter-granular-matrix/binder cracking/debonding, and is influenced by global initial boundary value problem (IBVP) conditions. Discovering how these processes occur by experimental measurements is difficult because of their dynamic nature and the influence of global boundary conditions (BCs). Global BCs, such as lateral confinement on cylindrical compression specimens, can influence the resulting failure mode, generating in a glass ceramic composite axial splitting and fragmentation when there is no confinement and shear fractures with confinement (*4*). Thus, we resort to physics-based modeling to help uncover these origins dynamically.

Examples of bound particulate materials include, but are not limited to, the following: polycrystalline ceramics (crystalline grains with amorphous grain boundary phases, figure 1(a)), metal matrix composites (metallic grains with bulk amorphous metallic binder, figure 1(b)), particulate energetic materials (explosive crystalline grains with polymeric binder, figure 1(c)), asphalt pavement (stone/rubber aggregate with hardened binder, figure 1(d)), mortar (sand grains with cement binder), conventional quasi-brittle concrete (stone aggregate with cement binder), and sandstones (sand grains with clayey binder). Bound particulate materials contain grains (quasi-brittle or ductile) bound by binder material oftentimes called the "matrix." The heterogeneous particulate nature of these materials governs their mechanical behavior at the grain-to-macro-scales, especially in IBVPs for which localized deformation nucleates. Thus, grain-scale material model resolution is needed in regions of localized deformation nucleation (e.g., at a macro-crack tip, or at the high shear strain rate interface region between a projectile and target material[1]). To predict dynamic failure for realistic IBVPs, a modeling approach will need to account *simultaneously* for the underlying grain-scale physics and macro-scale continuum IBVP conditions.

Direct Numerical Simulation (DNS) represents directly the grain-scale mechanical behavior under static (*5*) and dynamic loading conditions (*6–8*). Currently, DNS is the best approach to understanding fundamentally dynamic material failure, but is deficient in the following ways:

[1]Both projectile and target material could be modeled with such grain-scale material model resolution at their interface region where significant fracture and comminution occurs.

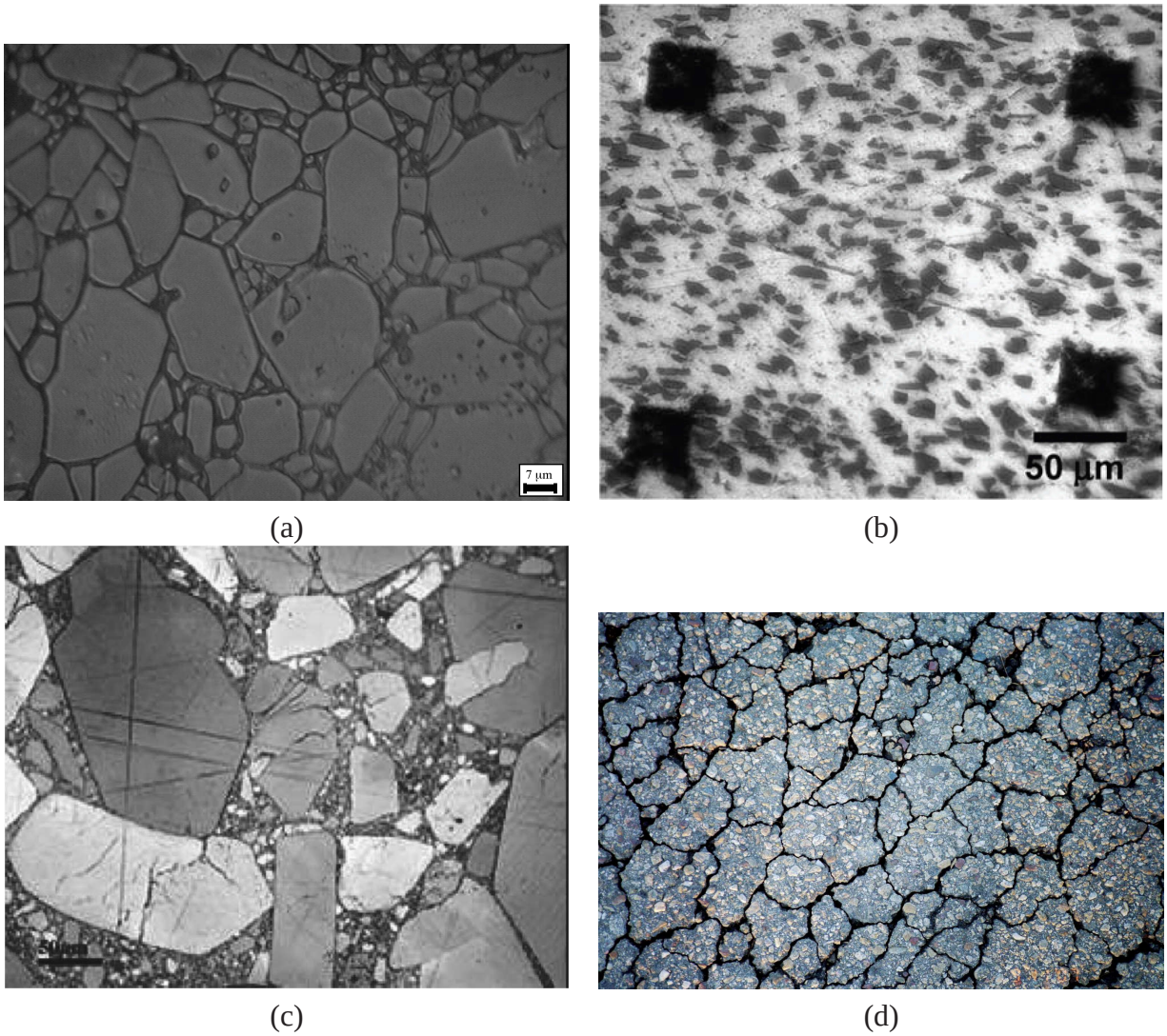

Figure 1. (a) Microstructure of alumina, composed of grains bound by glassy phase (Sandia). (b) SiC reinforced 2080 aluminum metal matrix composite (*1*). The four large black squares are indents to identify the region. (c) Cracking in explosive HMX grains and at grain-matrix interfaces (*2*). (d) Cracking in asphalt pavement.

(i) it is limited by current computing power (even massively-parallel computing) to a small representative volume element (RVE) of the material; and (ii) it usually must assume unrealistic BCs on the RVE (e.g., periodic, or prescribed uniform traction or displacement). Thus, multi-scale modeling techniques are needed to predict dynamic failure in bound particulate materials.

Current multi-scale approaches attempt to do this but fall short by one or more of the following limitations: (i) not providing proper BCs on the micro-structural DNS region; (ii) homogenizing at the macro-scale the underlying micro-structural response in the unit cell and, thus, not maintaining a computational 'open window' to model micro-structurally dynamic failure[2]; and (iii) not making these methods adaptive, i.e., moving a computational 'open window' with grain-scale model resolution over regions experiencing dynamic failure.

1.2 Proposed Approach

As a precursor to a three-dimensional (3D) finite strain micromorphic plasticity model (*9*) and finite element (FE) implementation (*10*), and overlap coupling with underlying 3D FE or discrete element (DE) DNS region, we consider a simpler, one dimensional (1D) problem: overlap coupling between a micropolar linear elastic 1D mixed FE model and a 1D string of Hertzian (*11, 12*) nonlinear elastic DE spheres.

To illustrate the application of the micromorphic plasticity model (of which micropolar elasticity is a subset) to the problem of interest, we refer to an illustration in figure 2 of a concurrent multiscale modeling framework for bound particulate materials (target) impacted by a deformable solid (projectile). The higher order continuum micromorphic plasticity model is used in the overlap region between a continuum finite element (FE) and DNS representation of the particulate material. The additional degrees of freedom provided by the micromorphic model (micro-shear, micro-dilation/compaction, and micro-rotation) will allow the overlap region to be placed closer to the region of interest, such as at a projectile-target interface. Further from this interface region, standard continuum mechanics and constitutive models can be used. The discrete element (DE) and/or finite element (FE) representation of the particulate micro-structure is intentionally not shown in order not to clutter the drawing of the micro-structure. The grains (binder matrix not shown) of the micro-structure are 'meshed' using DEs and/or FEs with cohesive surface elements (CSEs). The open circles denote continuum FE nodes that have prescribed degrees of freedom (dofs) $\widehat{\boldsymbol{D}}$ based on the underlying grain-scale response, while the solid circles denote continuum FE nodes that have free dofs $\boldsymbol{D}$ governed by the micromorphic continuum model. We

[2]This is a problem especially for modeling fragmentation and comminution micro-structurally.

intentionally leave an 'open window' (i.e., DNS) on the particulate micro-structural mesh in order to model dynamic failure. If the continuum mesh overlays the whole particulate micro-structural region, as in (*13*) for atomistic-continuum coupling, then the continuum FEs would eventually become too deformed by following the micro-structural motion during fragmentation. The blue-dashed box at the bottom-center of the illustration is a micromorphic continuum FE region that can be converted to a DNS region for adaptive high-fidelity material modeling as the projectile penetrates the target.

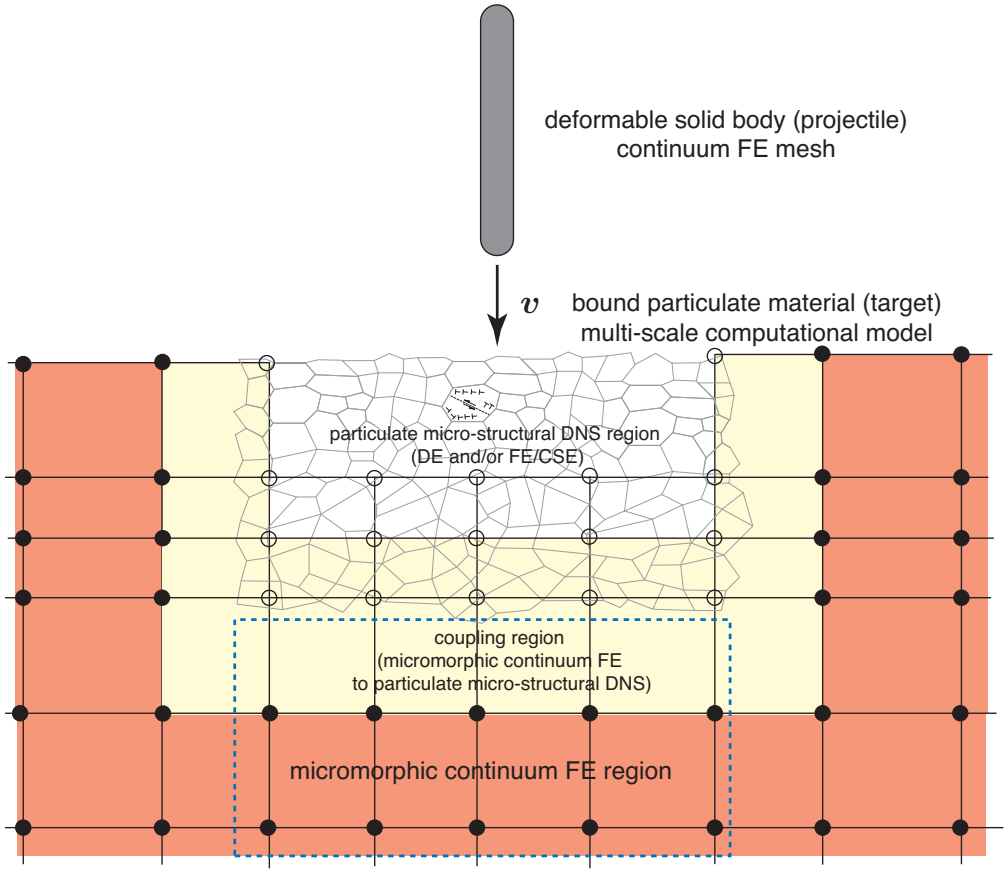

Figure 2. 2D illustration of concurrent computational multi-scale modeling approach in the contact interface region between a bound particulate material (e.g., ceramic target) and deformable solid body (e.g., refractory metal projectile).

1.3 Focus of Report

Regarding the approach described in section 1.2, this report focusses on the 1D overlap coupling between a micropolar linear elastic FE model and a 1D string of Hertzian nonlinear elastic DE spheres. An outline of the report is as follows: section 2.1 summarizes the Statement of Work (SOW) and the Tasks, section 2.2 the 1D micropolar linear elasticity derived from the 3D micropolar theory using Timoshenko beam kinematics with axial stretch, section 2.3 the

nonlinear elastic theory and implementation for spherical DE particles with Hertzian elastic contact, section 2.4 the overlap coupling methodology and numerical examples, and section 3. summarizes the results, conclusions, and future work.

The DE-FE coupled implementation is currently limited to nonlinear quasi-statics, but the formulation has been provided in general for nonlinear dynamics, and will be extended to dynamics in future work.

1.4 Notation

Index notation will be used wherever needed to clarify the presentation. Cartesian coordinates are assumed, so all indices are subscripts, and spatial partial derivative is the same as covariant derivative (*14*). Some symbolic/direct notation is also given, such that $(\boldsymbol{ab})_{ik} = a_{ij}b_{jk}$, $(\boldsymbol{a} \otimes \boldsymbol{b})_{ijkl} = a_{ij}b_{kl}$. Boldface denotes a tensor or vector, where its index notation is given. Subscript $(\bullet)_{,i}$ implies a spatial partial derivative. Superposed dot $(\dot{\square}) = D(\square)/Dt$ denotes material time derivative. The symbol $\stackrel{\text{def}}{=}$ implies a definition.

2. Technical Discussion

2.1 Statement of Work (SOW) and Specific Tasks

Bound particulate materials are commonly found in industrial products, construction materials, and nature (e.g., geological materials). They include polycrystalline ceramics (e.g., crystalline grains with amorphous grain boundary phases), energetic materials (high explosives and solid rocket propellant), hot asphalt, asphalt pavement (after asphalt has cured), mortar, conventional quasi-brittle concrete, ductile fiber composite concretes, and sandstones, for instance. Bound particulate materials contain particles[3] (quasi-brittle or ductile) bound by binder material oftentimes called the "matrix".

The heterogeneous nature of bound particulate materials governs its mechanical behavior at the particle- to continuum-scales. The particle-scale is denoted as the scale at which particle-matrix mechanical behavior is dominant, thus necessitating that particles and matrix material be resolved explicitly (i.e., meshed directly in a numerical model), accounting for their interfaces and differences in material properties. Currently, there is no approach enabling prediction of initiation and propagation of dynamic fracture in bound particulate materials—for example, polycrystalline ceramics, particulate energetic materials, mortar, and sandstone—accounting for their underlying particulate microstructure across multiple length-scales concurrently. Traditional continuum methods have provided the basis for understanding the dynamic fracture of these materials, but cannot predict the initiation of dynamic fracture without accounting for the material's particulate nature. Direct numerical simulation (DNS) of deformation, intra-particle cracking, and inter-particle-matrix/binder debonding at the particle-scale is limited by current computing power (even massively-parallel computing) to a small representative volume element (RVE) of the material, and usually must assume overly-restrictive boundary conditions (BCs) on the RVE (e.g., fixed normal displacement).

Multiscale modeling techniques are clearly needed to accurately capture the response of bound particulate materials in a way accounting simultaneously for effects of the microstructure at the particle-scale and boundary conditions applied to the engineering structure of interest, at the continuum-scale. The services of a scientist or engineer are required to develop the mathematical theory and numerical methodology for multiscale modeling of bound particulate materials of interest to the U.S. Army Research Laboratory (ARL).

[3] We use 'particle' and 'grain' interchangeably.

The overall objective of the proposed research is to develop a concurrent multi-scale computational modeling approach that couples regions of continuum deformation to regions of particle-matrix deformation, cracking, and debonding, while bridging the particle- to continuum-scale mechanics to allow numerical adaptivity in modeling initiation of dynamic fracture and degradation in bound particulate materials.

For computational efficiency, the solicited research will use DNS only in spatial regions of interest, such as the initiation site of a crack and its tip during propagation, and a micromorphic continuum approach will be used in the overlap and adjacent regions to provide proper BCs on the DNS region, as well as an overlay continuum to which to project the underlying particle-scale mechanical response (stress, internal state variables (ISVs)). The micromorphic continuum constitutive model will account for the inherent length scale of damaged fracture zone at the particle-scale, and, thus, includes the kinematics to enable the proper coupling with the fractured DNS particle region. Outside of the DNS region, a micromorphic extension of existing continuum model(s), with the particular model(s) to be determined based on ARL needs, of material behavior will be used.

This SOW calls for development of the formulation and finite element implementation of a finite strain micromorphic inelastic constitutive model to bridge particle-scale mechanics to the continuum-scale. The desired result is formulation of such a model, enabling a more complete understanding of the role of microstructure-scale physics on the thermomechanical properties and performance of heterogeneous materials of interest to ARL. These materials could include, but are not limited to, the following: ceramic materials, energetic materials, geological materials, and urban structural materials.

2.1.1 Specific Tasks

What follows is a list of specific tasks, and a summary of what was accomplished for each task.

1. *Finite element implementation of finite strain micromorphic pressure-sensitive elasto-plasticity model (Regueiro, J. Eng. Mech., 2009) in the continuum mechanics code Tahoe* `sourceforge.net/projects/tahoe`.

   This implementation is ongoing, but has not been completed in time for this report.

2. *Interact with ARL researchers in order to improve mutual understanding with regards to dynamic fracture and material degradation in heterogeneous and particulate materials and associated numerical modeling techniques.*

Continue to interact with ARL researchers regarding their needs for this research problem.

3. *Refine formulation of algorithm to couple finite strain micromorphic continuum finite elements to DNS finite elements of bound particulate material through an overlapping region.*

   This has been accomplished to some extent through the 1D overlap coupling problem described in this report in sections 2.2, 2.3, and 2.4.

4. *Implement coupling algorithm in using finite element code Tahoe (both for micromorphic continuum and DNS). Extension can be made for coupling micromorphic model (Tahoe) to DNS model (ARL or other finite element, or particle/meshfree, code).*

   The coupling algorithm has been implemented in a separate standalone code instead of Tahoe. Future research will establish the coupling in Tahoe, as part of currently funded research projects.

2.2 One-dimensional (1D) Micropolar Linear Isotropic Elasticity

This section (in section 2.2.1) briefly presents the three-dimensional (3D), small strain, linear isotropic micropolar elasticity model and balance of linear and angular momentum equations based on the work of (*15*), and then provides more details on the reduction to a 1D form (section 2.2.2) using Timoshenko beam kinematics with axial stretch (*16*). Finally, in section 2.2.3, the 1D form of the model is expressed in weak and Galerkin forms for finite element implementation, a mixed 1D element is used to interpolate the fields, and a numerical example is presented to demonstrate convergence of the FE implementation.

2.2.1 Three-dimensional (3D) Micropolar Linear Isotropic Elasticity and Balance Equations

The balance of linear and angular momentum, respectively, for a micropolar continuum are (*15*)

$$\sigma_{lk,l} + \rho b_k - \rho \ddot{u}_k = 0 \tag{1}$$

$$m_{lk,l} + e_{kmn}\sigma_{mn} + \rho \ell_k - \rho \dot{\beta}_k = 0 \tag{2}$$

where σ_{lk} is the unsymmetric Cauchy stress tensor over body $\mathcal{B}$, ρ is the mass density, b_k is a body force per unit mass, u_k is the displacement vector, $\ddot{u}_k$ is the acceleration vector, m_{lk} is the unsymmetric couple stress, e_{kmn} is the permutation operator, ℓ_k is the body couple per unit mass,

$\beta_k = j\dot{\varphi}_k$ is the intrinsic spin per unit mass, j is the spin inertia for a spin-isotropic material (*17*), φ_l is the micro-rotation vector, indices $k, l, \cdots = 1, 2, 3$, and $(\bullet)_{,l} = \partial(\bullet)/\partial x_l$ denotes partial differentiation with respect to the coordinate x_l.

For a linear isotropic elastic micropolar solid, the constitutive equations are (*15*)

$$\sigma_{kl} = \lambda\epsilon_{rr}\delta_{kl} + (2\mu + \kappa)\epsilon_{kl} + \kappa e_{klm}(r_m - \varphi_m) \tag{3}$$

$$m_{kl} = \alpha\varphi_{r,r}\delta_{kl} + \beta\varphi_{k,l} + \gamma\varphi_{l,k} \tag{4}$$

where λ, μ, κ, α, β, and γ are isotropic elastic parameters, and the deformations are

$$\epsilon_{kl} = \frac{1}{2}(u_{k,l} + u_{l,k}) \tag{5}$$

$$r_k = \frac{1}{2}e_{klm}u_{m,l} \tag{6}$$

$$r_{kl} = \frac{1}{2}(u_{k,l} - u_{l,k}) = -e_{klm}r_m \tag{7}$$

where ϵ_{kl} is the classical small strain tensor, r_k the axial vector, and r_{kl} the rotation tensor.

2.2.2 1D Timoshenko Beam Kinematics with Axial Stretch and Resulting 1D Micropolar Linear Elasticity

We consider Timoshenko beam kinematics from (*16*), with superimposed axial stretch for small deformations. The displacement vector $\boldsymbol{u}$ and micro-rotation vector $\boldsymbol{\varphi}$ are

$$\boldsymbol{u} = \begin{bmatrix} u_1 \\ u_2 \\ u_3 \end{bmatrix} = \begin{bmatrix} u - x_2\theta \\ v \\ 0 \end{bmatrix}, \ \boldsymbol{\varphi} = \begin{bmatrix} \varphi_1 \\ \varphi_2 \\ \varphi_3 \end{bmatrix} = \begin{bmatrix} 0 \\ 0 \\ \theta \end{bmatrix} \tag{8}$$

where u is the stretch in the x_1 direction, θ is the rotation of the centroidal axis about the x_3 axis, v is the transverse displacement in the x_2 direction, we ignore displacement $w \approx 0$ in the x_3 direction, and we assume the micro-rotation $\varphi_3 \stackrel{\text{def}}{=} \theta$.

Taking spatial derivatives, we have the following deformation measures:

$$[u_{k,l}] = \begin{bmatrix} \frac{\partial u}{\partial x_1} - x_2\frac{\partial \theta}{\partial x_1} & -\theta & 0 \\ \frac{\partial v}{\partial x_1} & 0 & 0 \\ 0 & 0 & 0 \end{bmatrix}, \; [\epsilon_{k,l}] = \begin{bmatrix} \frac{\partial u}{\partial x_1} - x_2\frac{\partial \theta}{\partial x_1} & \frac{1}{2}\left(\frac{\partial v}{\partial x_1} - \theta\right) & 0 \\ \frac{1}{2}\left(\frac{\partial v}{\partial x_1} - \theta\right) & 0 & 0 \\ 0 & 0 & 0 \end{bmatrix} \tag{9}$$

$$[r_k] = \frac{1}{2}[e_{klm}u_{m,l}] = \begin{bmatrix} 0 \\ 0 \\ \frac{1}{2}\left(\frac{\partial v}{\partial x_1} + \theta\right) \end{bmatrix}$$

$$[r_{kl}] = -[e_{klm}r_m] = \begin{bmatrix} 0 & -\frac{1}{2}\left(\frac{\partial v}{\partial x_1} + \theta\right) & 0 \\ \frac{1}{2}\left(\frac{\partial v}{\partial x_1} + \theta\right) & 0 & 0 \\ 0 & 0 & 0 \end{bmatrix} \tag{10}$$

$$[e_{klm}\varphi_m] = \begin{bmatrix} 0 & \theta & 0 \\ -\theta & 0 & 0 \\ 0 & 0 & 0 \end{bmatrix} \tag{11}$$

The unsymmetric stress tensor components then result as

$$\sigma_{11} = (\lambda + 2\mu + \kappa)\epsilon_{11} \tag{12}$$

$$\sigma_{22} = \lambda\epsilon_{11} \tag{13}$$

$$\sigma_{33} = \lambda\epsilon_{11} \tag{14}$$

$$\sigma_{12} = (2\mu + \kappa)\epsilon_{12} - \kappa r_{12} - \kappa e_{12m}\varphi_m = (\mu + \kappa)(\frac{\partial v}{\partial x_1} - \theta) = (\mu + \kappa)\gamma^{\mathrm{sh}} \tag{15}$$

$$\sigma_{21} = (2\mu + \kappa)\epsilon_{21} - \kappa r_{21} - \kappa e_{21m}\varphi_m = \mu\gamma^{\mathrm{sh}} \tag{16}$$

$$m_{13} = \gamma\frac{\partial \theta}{\partial x_1} \tag{17}$$

$$m_{31} = \beta\frac{\partial \theta}{\partial x_1} \tag{18}$$

where $\gamma^{\mathrm{sh}} \stackrel{\mathrm{def}}{=} \frac{\partial v}{\partial x_1} - \theta$, $\sigma_{23} = \sigma_{32} = \sigma_{13} = \sigma_{31} = 0$, and
$m_{11} = m_{22} = m_{33} = m_{12} = m_{21} = m_{23} = m_{32} = 0$.

The balance of linear and angular momentum equations can likewise be reduced as

$$\sigma_{11,1} - \rho\ddot{u}_1 = 0 \tag{19}$$

$$\sigma_{12,1} - \rho\ddot{u}_2 = 0 \tag{20}$$

$$m_{13,1} + \sigma_{12} - \sigma_{21} - \rho\dot{\beta}_3 = 0 \tag{21}$$

where $\dot{\beta}_3 = j\ddot{\varphi}_3 = j\ddot{\theta}$, assuming spin-inertia j is constant at small strains. However, to reach a form amenable to a 1D mixed FE formulation, we express the weak form in terms of the reduced kinematics. Consider the weak form in 3D as

$$\int_{\mathcal{B}} \rho w_k \ddot{u}_k dv + \int_{\mathcal{B}} w_{k,l}\sigma_{lk} dv = \int_{\Gamma_t} w_k t_k da \tag{22}$$

$$\int_{\mathcal{B}} \rho \eta_k \dot{\beta}_k dv + \int_{\mathcal{B}} \eta_{k,l} m_{lk} dv - \int_{\mathcal{B}} \eta_k e_{kmn}\sigma_{mn} dv = \int_{\Gamma_r} \eta_k r_k da \tag{23}$$

where the traction $t_k = \sigma_{lk}n_l$, surface couple stress $r_k = m_{lk}n_l$, and the weighting functions are

$$[w_k] = \begin{bmatrix} w_1 \\ w_2 \\ 0 \end{bmatrix} = \begin{bmatrix} \delta u_1 \\ \delta u_2 \\ 0 \end{bmatrix} = \begin{bmatrix} \delta u - x_2\delta\theta \\ \delta v \\ 0 \end{bmatrix} \tag{24}$$

$$[\eta_k] = \begin{bmatrix} 0 \\ 0 \\ \eta_3 \end{bmatrix} = \begin{bmatrix} 0 \\ 0 \\ \delta\varphi_3 \end{bmatrix} = \begin{bmatrix} 0 \\ 0 \\ \delta\theta \end{bmatrix} \tag{25}$$

where $\delta(\bullet)$ is used here as a variational operator. Likewise, $\ddot{u}_1 = \ddot{u} - x_2\ddot{\theta}$ and $\ddot{u}_2 = \ddot{v}$. We analyze each term separately, such that the first term of equation 22 is

$$\int_{\mathcal{B}} \rho w_k \ddot{u}_k dv = \int_{\mathcal{B}} \rho(w_1\ddot{u}_1 + w_2\ddot{u}_2) dv \tag{26}$$

$$= \int_{\mathcal{B}} \rho \left[\delta u(\ddot{u} - x_2\ddot{\theta}) + \delta v(\ddot{v}) + \delta\theta(-x_2\ddot{u} + (x_2)^2\ddot{\theta})\right] dv \tag{27}$$

where we consider that all variables are functions only along the 1-D length x_1 (which we will simplify as x).

Thus, when reducing the integral $\int_{\mathcal{B}}(\bullet)dv = \int_L \int_A (\bullet) da dx$, we have

$$\int_{\mathcal{B}} \rho w_k \ddot{u}_k dv \;=\; \int_L \left[\delta u(\rho A\ddot{u} - \rho Q\ddot{\theta}) + \delta v(\rho A\ddot{v}) + \delta\theta(-\rho Q\ddot{u} + \rho I\ddot{\theta})\right] dx \tag{28}$$

where, the first moment about the x_1 axis Q and moment of inertia about x_1 axis I are defined as

$$Q \stackrel{\text{def}}{=} \int_A x_2 da \;, \quad I \stackrel{\text{def}}{=} \int_A (x_2)^2 da \tag{29}$$

Likewise, the stress term is

$$\begin{aligned}
\int_{\mathcal{B}} w_{k,l}\sigma_{lk} dv \;&=\; \int_{\mathcal{B}} (w_{1,1}\sigma_{11} + w_{2,1}\sigma_{12}) dv && (30)\\
&=\; \int_L [\delta u_{,x}(\lambda + 2\mu + \kappa)(Au_{,x} - Q\theta_{,x}) + \delta v_{,x}(\mu + \kappa)A(v_{,x} - \theta) \\
&\quad +\delta\theta_{,x}(\lambda + 2\mu + \kappa)(-Qu_{,x} + I\theta_{,x})]\, dx && (31)
\end{aligned}$$

Considering that the traction acts in the x_1 direction on the x_1 face, then the unit normal to Γ_t is $\boldsymbol{n} = [1\,0\,0]^T$, and $t_1 = \sigma_{11}$, $t_2 = \sigma_{12}$. Then,

$$\begin{aligned}
\int_{\Gamma_t} w_k t_k da \;&=\; \int_A (w_1 t_1 + w_2 t_2) da && (32)\\
&=\; \int_A \delta u\sigma_{11} da - \int_A \delta\theta x_2 \sigma_{11} da + \int_A \delta v \sigma_{12} da && (33)
\end{aligned}$$

where, if we consider the traction acts at $x = L$, then concentrated axial force $F_L = \int_A \sigma_{11} da$, end moment $-M_L = \int_A x_2\sigma_{11} da$, and end shear force $V_L = \int_A \sigma_{12} dA$, and, thus,

$$\int_{\Gamma_t} w_k t_k da \;=\; \delta u_L F_L + \delta\theta_L M_L + \delta v_L V_L \tag{34}$$

For the balance of angular momentum weak form, we have for the micro-inertia term

$$\int_{\mathcal{B}} \rho\eta_k \dot{\beta}_k dv \;=\; \int_L \delta\theta(\rho A j\ddot{\theta}) dx \tag{35}$$

and for the couple stress term

$$\int_{\mathcal{B}} \eta_{k,l} m_{lk} dv \;\; = \;\; \int_{\mathcal{B}} \eta_{3,1} m_{13} dv = \int_L \delta\theta_{,x} (\gamma A \theta_{,x}) dx \tag{36}$$

and the skew part of the stress

$$-\int_{\mathcal{B}} \eta_k e_{kmn} \sigma_{mn} dv \;\; = \;\; \int_{\mathcal{B}} \delta\theta(\sigma_{12} - \sigma_{21}) dv = \int_L \delta\theta \left[\kappa A(\theta - v_{,x})\right] dx \tag{37}$$

where if the traction couple stress acts on the x_1 face at $x = L$, then

$$\int_{\Gamma_r} \eta_k r_k da \;\; = \;\; \int_A \delta\theta m_{13} da = \delta\theta_L M_L^\theta \,, \quad M_L^\theta = \int_A m_{13} da \tag{38}$$

Next, we put these equations in Finite Element (FE) matrix form.

2.2.3 Finite Element (FE) Implementation of 1D Micropolar Linear Elasticity

The Galerkin form of the reduced equations may be written as

$$\begin{aligned}
&\int_L \Big[\delta u^h(\rho A \ddot{u}^h - \rho Q \ddot{\theta}^h) + \delta v^h(\rho A \ddot{v}^h) + \delta\theta^h(-\rho Q \ddot{u}^h + \rho I \ddot{\theta}^h) \\
&\delta u^h_{,x}(\lambda + 2\mu + \kappa)(A u^h_{,x} - Q\theta^h_{,x}) + \delta v^h_{,x}(\mu + \kappa) A(v^h_{,x} - \theta^h) \\
&+\delta\theta^h_{,x}(\lambda + 2\mu + \kappa)(-Q u^h_{,x} + I\theta^h_{,x})\Big] \, dx = \delta u^h_L F_L + \delta\theta^h_L M_L + \delta v^h_L V_L
\end{aligned} \tag{39}$$

$$\int_L \left[\delta\theta^h(\rho A j \ddot{\theta}^h) + \delta\theta^h_{,x}(\gamma A \theta^h_{,x}) + \delta\theta^h \left[\kappa A(\theta^h - v^h_{,x})\right]\right] dx = \delta\theta^h_L M^\theta_L \tag{40}$$

The interpolations, and their spatial derivatives, for a mixed element shown in figure 3 are the following

$$
\begin{aligned}
u^h(\xi) &= \sum_{a=1}^{2} N_a^u(\xi) d^e_{x(a)} = \left[\begin{array}{cc} N_1^u & N_2^u \end{array}\right] \left[\begin{array}{c} d^e_{x(1)} \\ d^e_{x(2)} \end{array}\right] = \boldsymbol{N}^{u,e}\boldsymbol{d}^e_x \\
v^h(\xi) &= \sum_{a=1}^{2} N_a^v(\xi) d^e_{y(a)} = \left[\begin{array}{ccc} N_1^v & N_2^v & N_3^v \end{array}\right] \left[\begin{array}{c} d^e_{y(1)} \\ d^e_{y(2)} \\ d^e_{y(3)} \end{array}\right] = \boldsymbol{N}^{v,e}\boldsymbol{d}^e_y \\
\theta^h(\xi) &= \sum_{a=1}^{2} N_a^\theta(\xi) d^e_{\theta(a)} = \left[\begin{array}{cc} N_1^\theta & N_2^\theta \end{array}\right] \left[\begin{array}{c} d^e_{\theta(1)} \\ d^e_{\theta(2)} \end{array}\right] = \boldsymbol{N}^{\theta,e}\boldsymbol{d}^e_\theta \\
\delta u^h(\xi) &= \boldsymbol{N}^{u,e}\boldsymbol{c}^e_x \\
\delta v^h(\xi) &= \boldsymbol{N}^{v,e}\boldsymbol{c}^e_y \\
\delta \theta^h(\xi) &= \boldsymbol{N}^{\theta,e}\boldsymbol{c}^e_\theta \\
u^h(\xi)_{,x} &= \boldsymbol{B}^{u,e}\boldsymbol{d}^e_x\,, \quad \boldsymbol{B}^{u,e} = \left[\begin{array}{cc} N^u_{1,x} & N^u_{2,x} \end{array}\right] \\
v^h(\xi)_{,x} &= \boldsymbol{B}^{v,e}\boldsymbol{d}^e_y\,, \quad \boldsymbol{B}^{v,e} = \left[\begin{array}{ccc} N^v_{1,x} & N^v_{2,x} & N^v_{3,x} \end{array}\right] \\
\theta^h(\xi)_{,x} &= \boldsymbol{B}^{\theta,e}\boldsymbol{d}^e_\theta\,, \quad \boldsymbol{B}^{\theta,e} = \left[\begin{array}{cc} N^\theta_{1,x} & N^\theta_{2,x} \end{array}\right] \\
\delta u^h(\xi)_{,x} &= \boldsymbol{B}^{u,e}\boldsymbol{c}^e_x \\
\delta v^h(\xi)_{,x} &= \boldsymbol{B}^{v,e}\boldsymbol{c}^e_y \\
\delta \theta^h(\xi)_{,x} &= \boldsymbol{B}^{\theta,e}\boldsymbol{c}^e_\theta
\end{aligned}
$$

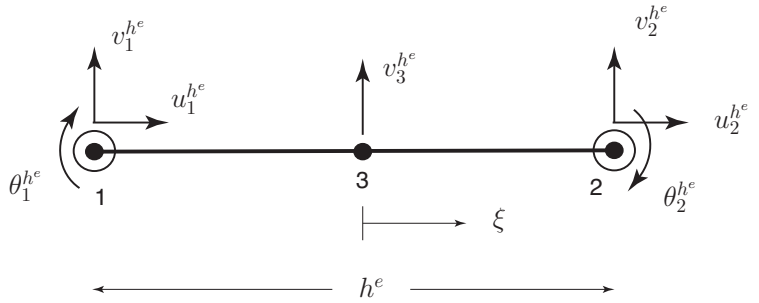

Figure 3. Finite element degrees of freedom (dof) for mixed formulation Timoshenko beam with axial stretch. The middle node 3 is at the center of the element, i.e., at $\xi = 0$, where ξ is the natural coordinate (*3*).

We assign $\boldsymbol{N}^{\theta,e} = \boldsymbol{N}^{u,e}$ and $\boldsymbol{B}^{\theta,e} = \boldsymbol{B}^{u,e}$, and the element dofs are

$$\begin{bmatrix} u_1^{h^e} \\ u_2^{h^e} \\ v_1^{h^e} \\ v_2^{h^e} \\ v_3^{h^e} \\ \theta_1^{h^e} \\ \theta_2^{h^e} \end{bmatrix} = \boldsymbol{d}^e = \begin{bmatrix} d^e_{x(1)} \\ d^e_{x(2)} \\ d^e_{y(1)} \\ d^e_{y(2)} \\ d^e_{y(3)} \\ d^e_{\theta(1)} \\ d^e_{\theta(2)} \end{bmatrix} = \begin{bmatrix} \boldsymbol{d}^e_x \\ \boldsymbol{d}^e_y \\ \boldsymbol{d}^e_\theta \end{bmatrix} \tag{41}$$

Substituting these interpolations into the Galerkin form of balance of linear momentum in equation 39, and grouping terms, we can define element mass and stiffness matrices as

$$\begin{aligned}
&\mathop{\mathsf{A}}_{e=1}^{n_{\text{el}}} (\boldsymbol{c}_x^e)^T \Bigg[\underbrace{\left(\int_{\ell^e} \rho A^e (\boldsymbol{N}^{u,e})^T \boldsymbol{N}^{u,e} dx \right)}_{\boldsymbol{m}^{uu,e}} \ddot{\boldsymbol{d}}_x^e - \underbrace{\left(\int_{\ell^e} \rho Q^e (\boldsymbol{N}^{u,e})^T \boldsymbol{N}^{\theta,e} dx \right)}_{\boldsymbol{m}^{u\theta,e}} \ddot{\boldsymbol{d}}_\theta^e \\
&+ \underbrace{\left(\int_{\ell^e} (\lambda + 2\mu + \kappa) A^e (\boldsymbol{B}^{u,e})^T \boldsymbol{B}^{u,e} dx \right)}_{\boldsymbol{k}^{uu,e}} \boldsymbol{d}_x^e - \underbrace{\left(\int_{\ell^e} (\lambda + 2\mu + \kappa) Q^e (\boldsymbol{B}^{u,e})^T \boldsymbol{B}^{\theta,e} dx \right)}_{\boldsymbol{k}^{u\theta,e}} \boldsymbol{d}_\theta^e \\
&= \boldsymbol{f}_F^e \Bigg]
\end{aligned} \tag{42}$$

$$\begin{aligned}
&\mathop{\mathsf{A}}_{e=1}^{n_{\text{el}}} (\boldsymbol{c}_y^e)^T \Bigg[\underbrace{\left(\int_{\ell^e} \rho A^e (\boldsymbol{N}^{v,e})^T \boldsymbol{N}^{v,e} dx \right)}_{\boldsymbol{m}^{vv,e}} \ddot{\boldsymbol{d}}_y^e + \underbrace{\left(\int_{\ell^e} (\mu + \kappa) A^e (\boldsymbol{B}^{v,e})^T \boldsymbol{B}^{v,e} dx \right)}_{\boldsymbol{k}^{vv,e}} \boldsymbol{d}_y^e \\
&- \underbrace{\left(\int_{\ell^e} (\mu + \kappa) A^e (\boldsymbol{B}^{v,e})^T \boldsymbol{N}^{\theta,e} dx \right)}_{\boldsymbol{k}^{v\theta,e}} \boldsymbol{d}_\theta^e = \boldsymbol{f}_V^e \Bigg]
\end{aligned} \tag{43}$$

$$\begin{aligned}
&\mathop{\mathsf{A}}_{e=1}^{n_{\text{el}}} (\boldsymbol{c}_\theta^e)^T \Bigg[- \underbrace{\left(\int_{\ell^e} \rho Q^e (\boldsymbol{N}^{\theta,e})^T \boldsymbol{N}^{u,e} dx \right)}_{\boldsymbol{m}^{\theta u,e}} \ddot{\boldsymbol{d}}_x^e + \underbrace{\left(\int_{\ell^e} \rho I^e (\boldsymbol{N}^{\theta,e})^T \boldsymbol{N}^{\theta,e} dx \right)}_{\boldsymbol{m}^{\theta\theta 1,e}} \ddot{\boldsymbol{d}}_\theta^e \\
&- \underbrace{\left(\int_{\ell^e} (\lambda + 2\mu + \kappa) Q^e (\boldsymbol{B}^{\theta,e})^T \boldsymbol{B}^{u,e} dx \right)}_{\boldsymbol{k}^{\theta u,e}} \boldsymbol{d}_x^e + \underbrace{\left(\int_{\ell^e} (\lambda + 2\mu + \kappa) I^e (\boldsymbol{B}^{\theta,e})^T \boldsymbol{B}^{\theta,e} dx \right)}_{\boldsymbol{k}^{\theta\theta 1,e}} \boldsymbol{d}_\theta^e \\
&= \boldsymbol{f}_M^e \Bigg]
\end{aligned} \tag{44}$$

where $\mathbf{A}$ is the element assembly operator, n_{el} the number of elements, and $\ell^e = h^e$ the length of an element e, where the equations can be written more concisely in matrix form as

$$\mathop{\mathbf{A}}_{e=1}^{n_{\text{el}}} (\boldsymbol{c}_x^e)^T \left[\boldsymbol{m}^{uu,e} \ddot{\boldsymbol{d}}_x^e - \boldsymbol{m}^{u\theta,e} \ddot{\boldsymbol{d}}_\theta^e + \boldsymbol{k}^{uu,e} \boldsymbol{d}_x^e - \boldsymbol{k}^{u\theta,e} \boldsymbol{d}_\theta^e = \boldsymbol{f}_F^e \right] \tag{45}$$

$$\mathop{\mathbf{A}}_{e=1}^{n_{\text{el}}} (\boldsymbol{c}_y^e)^T \left[\boldsymbol{m}^{vv,e} \ddot{\boldsymbol{d}}_y^e + \boldsymbol{k}^{vv,e} \boldsymbol{d}_y^e - \boldsymbol{k}^{v\theta,e} \boldsymbol{d}_\theta^e = \boldsymbol{f}_V^e \right] \tag{46}$$

$$\mathop{\mathbf{A}}_{e=1}^{n_{\text{el}}} (\boldsymbol{c}_\theta^e)^T \left[-\boldsymbol{m}^{\theta u,e} \ddot{\boldsymbol{d}}_x^e + \boldsymbol{m}^{\theta\theta 1,e} \ddot{\boldsymbol{d}}_\theta^e - \boldsymbol{k}^{\theta u,e} \boldsymbol{d}_x^e + \boldsymbol{k}^{\theta\theta 1,e} \boldsymbol{d}_\theta^e = \boldsymbol{f}_M^e \right] \tag{47}$$

Likewise, when substituting the interpolations into the Galerkin form of balance of angular momentum in equation 40, and grouping terms, we have

$$\begin{aligned} \mathop{\mathbf{A}}_{e=1}^{n_{\text{el}}} (\boldsymbol{c}_\theta^e)^T \Bigg[& \underbrace{\left(\int_{\ell^e} \rho j^e (\boldsymbol{N}^{\theta,e})^T \boldsymbol{N}^{\theta,e} dx \right)}_{\boldsymbol{m}^{\theta\theta 2,e}} \ddot{\boldsymbol{d}}_\theta^e + \underbrace{\left(\int_{\ell^e} \gamma A^e (\boldsymbol{B}^{\theta,e})^T \boldsymbol{B}^{\theta,e} dx \right)}_{\boldsymbol{k}^{\theta\theta 2,e}} \boldsymbol{d}_\theta^e \\ & + \underbrace{\left(\int_{\ell^e} \kappa A^e (\boldsymbol{N}^{\theta,e})^T \boldsymbol{N}^{\theta,e} dx \right)}_{\boldsymbol{k}^{\theta\theta 3,e}} \boldsymbol{d}_\theta^e - \underbrace{\left(\int_{\ell^e} \kappa A^e (\boldsymbol{N}^{\theta,e})^T \boldsymbol{B}^{v,e} dx \right)}_{\boldsymbol{k}^{\theta v,e}} \boldsymbol{d}_y^e = \boldsymbol{f}_{M^\theta}^e \Bigg] \end{aligned} \tag{48}$$

where, in summary, we have

$$\mathop{\mathbf{A}}_{e=1}^{n_{\text{el}}} (\boldsymbol{c}_\theta^e)^T \left[\boldsymbol{m}^{\theta\theta 2,e} \ddot{\boldsymbol{d}}_\theta^e + \boldsymbol{k}^{\theta\theta 2,e} \boldsymbol{d}_\theta^e + \boldsymbol{k}^{\theta\theta 3,e} \boldsymbol{d}_\theta^e - \boldsymbol{k}^{\theta v,e} \boldsymbol{d}_y^e = \boldsymbol{f}_{M^\theta}^e \right] \tag{49}$$

Adding equations 47 and 49 for the micro-rotation dofs, we have

$$\begin{aligned} \mathop{\mathbf{A}}_{e=1}^{n_{\text{el}}} (\boldsymbol{c}_\theta^e)^T \Big[& -\boldsymbol{m}^{\theta u,e} \ddot{\boldsymbol{d}}_x^e + (\boldsymbol{m}^{\theta\theta 1,e} + \boldsymbol{m}^{\theta\theta 2,e}) \ddot{\boldsymbol{d}}_\theta^e - \boldsymbol{k}^{\theta u,e} \boldsymbol{d}_x^e + (\boldsymbol{k}^{\theta\theta 1,e} + \boldsymbol{k}^{\theta\theta 2,e} + \boldsymbol{k}^{\theta\theta 3,e}) \boldsymbol{d}_\theta^e \\ & - \boldsymbol{k}^{\theta v,e} \boldsymbol{d}_y^e = \boldsymbol{f}_M^e + \boldsymbol{f}_{M^\theta}^e \Big] \end{aligned} \tag{50}$$

Accounting for essential boundary conditions (BCs), and assembling the global FE matrix equations (*3*), we arrive at the coupled system of matrix FE equations to solve for the unknown dofs as

$$
\begin{aligned}
&\boldsymbol{M}^D\ddot{\boldsymbol{D}} + \boldsymbol{K}^D\boldsymbol{D} = \boldsymbol{F}^D \qquad (51)\\
&\boldsymbol{D} = \begin{bmatrix} \boldsymbol{d}_x \\ \boldsymbol{d}_y \\ \boldsymbol{d}_\theta \end{bmatrix}, \quad \ddot{\boldsymbol{D}} = \begin{bmatrix} \ddot{\boldsymbol{d}}_x \\ \ddot{\boldsymbol{d}}_y \\ \ddot{\boldsymbol{d}}_\theta \end{bmatrix}, \quad \boldsymbol{F}^D = \begin{bmatrix} \boldsymbol{F}_F \\ \boldsymbol{F}_V \\ \boldsymbol{F}_M + \boldsymbol{F}_{M^\theta} \end{bmatrix}\\
&\boldsymbol{M}^D = \begin{bmatrix} \boldsymbol{M}^{uu} & \boldsymbol{0} & -\boldsymbol{M}^{u\theta} \\ \boldsymbol{0} & \boldsymbol{M}^{vv} & \boldsymbol{0} \\ -\boldsymbol{M}^{\theta u} & \boldsymbol{0} & \boldsymbol{M}^{\theta\theta} \end{bmatrix}\\
&\boldsymbol{K}^D = \begin{bmatrix} \boldsymbol{K}^{uu} & \boldsymbol{0} & -\boldsymbol{K}^{u\theta} \\ \boldsymbol{0} & \boldsymbol{K}^{vv} & -\boldsymbol{K}^{v\theta} \\ -\boldsymbol{K}^{\theta u} & -\boldsymbol{K}^{\theta v} & \boldsymbol{K}^{\theta\theta} \end{bmatrix}
\end{aligned}
$$

Since $\boldsymbol{N}^{\theta,e} = \boldsymbol{N}^{u,e}$, then $\boldsymbol{M}^{\theta u} = \boldsymbol{M}^{u\theta}$ and $\boldsymbol{M}^D$ is symmetric, and since $\boldsymbol{B}^{\theta,e} = \boldsymbol{B}^{u,e}$ then $\boldsymbol{K}^{\theta u} = \boldsymbol{K}^{u\theta}$, but $\boldsymbol{K}^D$ is, in general, unsymmetric because $\mu > 0$ which leads to $\boldsymbol{K}^{\theta v} \neq \boldsymbol{K}^{v\theta}$.

Given the mixed 1D Timoshenko beam micropolar elastic finite element with axial stretch in figure 3, we can select specific shape functions, with resulting first spatial derivatives, as follows:

$$\boldsymbol{N}^{u,e} = \frac{1}{2}\begin{bmatrix} 1-\xi & 1+\xi \end{bmatrix}, \ \boldsymbol{B}^{u,e} = \frac{1}{h^e}\begin{bmatrix} -1 & 1 \end{bmatrix} \qquad (52)$$

$$\boldsymbol{N}^{v,e} = \begin{bmatrix} \frac{1}{2}\xi(\xi-1) & \frac{1}{2}\xi(\xi+1) & 1-\xi^2 \end{bmatrix}, \ \boldsymbol{B}^{v,e} = \frac{2}{h^e}\begin{bmatrix} \xi-\frac{1}{2} & \xi-\frac{1}{2} & -2\xi \end{bmatrix} \qquad (53)$$

where h^e is the element length.

With these element interpolation matrices $\boldsymbol{N}^e$ and 'strain-displacement' matrices $\boldsymbol{B}^e$, and a bar with circular cross-section such that the first moment $Q^e = 0$ (see section 2.2.4), we arrive at specific forms of the element stiffness matrices as

$$\boldsymbol{k}^{uu,e} = \frac{A^e}{h^e}(\lambda + 2\mu + \kappa)\begin{bmatrix} 1 & -1 \\ -1 & 1 \end{bmatrix}, \quad \boldsymbol{k}^{u\theta,e} = \boldsymbol{k}^{\theta u,e} = \boldsymbol{0} \tag{54}$$

$$\boldsymbol{k}^{vv,e} = \frac{2A^e}{h^e}(\mu + \kappa)\begin{bmatrix} \frac{7}{6} & \frac{1}{6} & -\frac{4}{3} \\ \frac{1}{6} & \frac{7}{6} & -\frac{4}{3} \\ -\frac{4}{3} & -\frac{4}{3} & \frac{8}{3} \end{bmatrix} \tag{55}$$

$$\boldsymbol{k}^{v\theta,e} = \frac{A^e}{2}(\mu + \kappa)\begin{bmatrix} -\frac{5}{3} & -\frac{1}{3} \\ \frac{1}{3} & \frac{5}{3} \\ \frac{4}{3} & -\frac{4}{3} \end{bmatrix}, \quad \boldsymbol{k}^{\theta v,e} = \frac{A^e}{2}\kappa\begin{bmatrix} -\frac{5}{3} & \frac{1}{3} & \frac{4}{3} \\ -\frac{1}{3} & \frac{5}{3} & -\frac{4}{3} \end{bmatrix} \tag{56}$$

$$\boldsymbol{k}^{\theta\theta 1,e} = \frac{I^e}{h^e}(\lambda + 2\mu + \kappa)\begin{bmatrix} 1 & -1 \\ -1 & 1 \end{bmatrix}, \quad \boldsymbol{k}^{\theta\theta 2,e} = \frac{A^e}{h^e}\gamma\begin{bmatrix} 1 & -1 \\ -1 & 1 \end{bmatrix} \tag{57}$$

$$\boldsymbol{k}^{\theta\theta 3,e} = \frac{A^e h^e}{6}\kappa\begin{bmatrix} 2 & 1 \\ 1 & 2 \end{bmatrix} \tag{58}$$

We can similarly derive the element mass matrices, but since our simulations are currently limited to quasi-static problems, we do not show all details for including the inertia terms. This is part of future work.

2.2.4 Convergence of 1D Micropolar Linear Elastic FE

In this section, we take the FE formulation and implementation from the previous section and test its convergence with regard to spatial discretization refinement (i.e., $h^e \to 0$). It is well known that in the thin limit the Timoshenko beam formulation will do a poor job calculating transverse displacement (*16*), because the classical equal interpolation ($\boldsymbol{N}^{u,e} = \boldsymbol{N}^{v,e}$, and $\boldsymbol{B}^{u,e} = \boldsymbol{B}^{v,e}$) element "locks" as the transverse shear strain approaches zero in the thin limit. Thus, we use the mixed formulation ($\boldsymbol{N}^{u,e} \neq \boldsymbol{N}^{v,e}$, and $\boldsymbol{B}^{u,e} \neq \boldsymbol{B}^{v,e}$) in figure 3 and reduced integration to alleviate this problem[4] (*16*). Figure 4 shows the five-element mesh, and the force versus displacement results for two-, five-, ten-, and twenty-element meshes. We can see that for the axial force and displacement, the result is the same for all meshes (as expected for small strain theory, where axial and transverse displacements are decoupled), whereas for the five-element

[4]We note that in our case the reduced integration gives us no added benefit, as the mixed formulation seems sufficient to address any potential locking. See results in figure 4.

mesh, for the transverse force and displacement, the results appear convergent. In the overlap coupling simulations in section 2.4, we will use the five-element mesh.

Each mesh is $L = 20$cm in length, with rod circular cross-section with radius $R = 0.5$cm, as shown in figure 4. The applied forces are $F_x^{EXT} = 1$kN, $F_y^{EXT} = 1$kN. For the elastic parameters, we use Young's modulus $E = 10$GPa, Poisson's ratio $\nu = 0.3$ (approximate for quartz), and approximate λ and μ as

$$\lambda = \frac{E\nu}{(1+\nu)(1-2\nu)} \,, \quad \mu = \frac{E}{2(1+\nu)} \tag{59}$$

even though λ and μ are *not* the Lamé parameters. We approximate $\kappa = 0.1\mu$, and $\gamma = (0.05)\ell^2\mu$, with elastic length scale $\ell = 1$cm. The cross-sectional area $A = \pi R^2 = 7.85$e-5 m^2, first moment about the x-axis $Q = 0$, and moment of inertia about the x-axis $I = \frac{1}{4}\pi R^4 = 4.9$e-10 m^4.

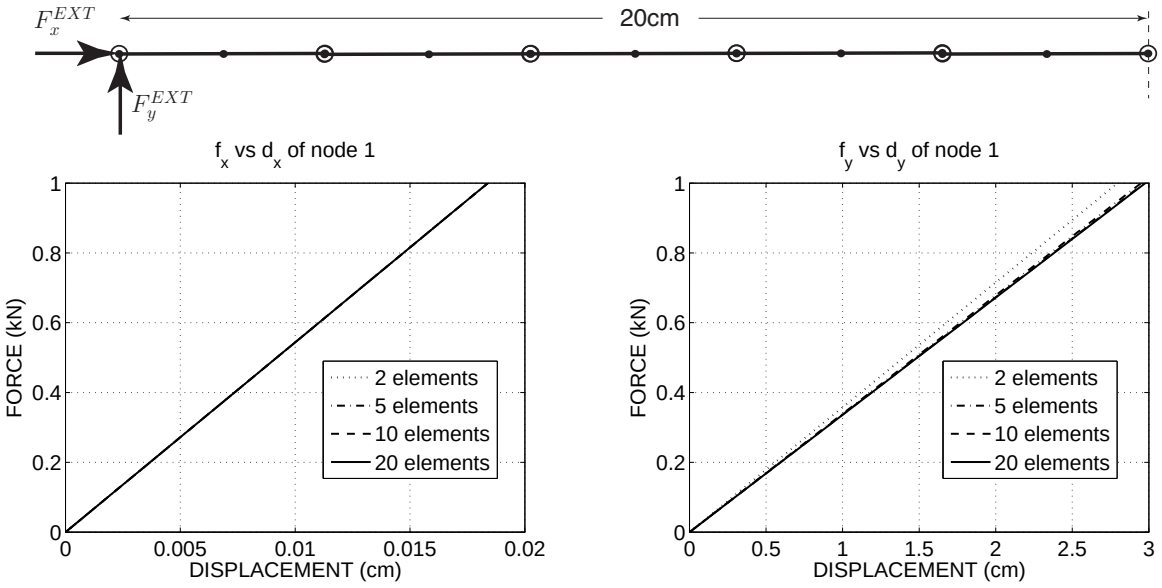

Figure 4. (top) Five-element mesh. (bottom) Demonstration of convergence of thin Timoshenko beam mixed FE implementation in compression, bending, and shear. Axial force versus displacement of the left end node is exact, whereas the two-element mesh may be too coarse, while the five-, ten-, and twenty-element meshes give nearly the same transverse displacement upon an applied transverse force F_y^{EXT}.

2.3 1D String of Hertzian Nonlinear Elastic Discrete Element (DE) Spheres

We refer to figure 5 for the kinematics and forces at contact ϵ between two discrete element (DE) spheres α and β. From Hertz-Mindlin elastic contact theory between stiff spheres (*11, 12, 18*), we have

$$\begin{aligned} f_x^\epsilon &= \frac{4}{3} E_0 R_0^{1/2} (\delta_n^\epsilon)^{3/2} \qquad (60) \\ & E_0 = \frac{E}{2(1-\nu^2)} \ , \ R_0 = R/2 \ , \ \delta_n^\epsilon = q_x^\alpha - q_x^\beta \\ f_y^\epsilon &= \frac{4\mu a}{2-\nu} \delta_t^\epsilon \qquad (61) \\ & \mu = \frac{E}{2(1+\nu)} \ , \ a = (\delta_n^\epsilon)^{1/2} \ , \ \delta_t^\epsilon = q_y^\alpha - q_y^\beta + R(\omega^\alpha + \omega^\beta) \end{aligned}$$

where E is the Young's modulus, ν is the Poisson's ratio, and R is the radius of a spherical particle (particles are assumed to have equal R in this case). We can then assemble the internal force vector $\boldsymbol{f}^{INT,\epsilon}$ and local consistent tangent $\partial \boldsymbol{f}^{INT,\epsilon} / \partial \boldsymbol{q}^\epsilon$ associated with dof vector $\boldsymbol{q}^\epsilon$ at contact ϵ as follows:

$$\boldsymbol{f}^{INT,\epsilon} = \begin{bmatrix} f_x^\epsilon \\ f_y^\epsilon \\ f_\omega^\epsilon \\ -f_x^\epsilon \\ -f_y^\epsilon \\ -f_\omega^\epsilon \end{bmatrix} \ , \quad \boldsymbol{q}^\epsilon = \begin{bmatrix} q_x^\alpha \\ q_y^\alpha \\ \omega^\alpha \\ q_x^\beta \\ q_y^\beta \\ \omega^\beta \end{bmatrix} \ , \quad \frac{\partial \boldsymbol{f}^{INT,\epsilon}}{\partial \boldsymbol{q}^\epsilon} = \begin{bmatrix} \frac{\partial f_x^\epsilon}{\partial \boldsymbol{q}^\epsilon} \\ \frac{\partial f_y^\epsilon}{\partial \boldsymbol{q}^\epsilon} \\ \frac{\partial f_\omega^\epsilon}{\partial \boldsymbol{q}^\epsilon} \\ -\frac{\partial f_x^\epsilon}{\partial \boldsymbol{q}^\epsilon} \\ -\frac{\partial f_y^\epsilon}{\partial \boldsymbol{q}^\epsilon} \\ -\frac{\partial f_\omega^\epsilon}{\partial \boldsymbol{q}^\epsilon} \end{bmatrix} \qquad (62)$$

$$\frac{\partial f_x^\epsilon}{\partial \boldsymbol{q}^\epsilon} = 2E_0 \sqrt{R_0} \sqrt{\delta_n^\epsilon} \frac{\partial \delta_n^\epsilon}{\partial \boldsymbol{q}^\epsilon} \ , \ \frac{\partial \delta_n^\epsilon}{\partial \boldsymbol{q}^\epsilon} = \begin{bmatrix} 1 & 0 & 0 & -1 & 0 & 0 \end{bmatrix} \qquad (63)$$

$$\frac{\partial f_y^\epsilon}{\partial \boldsymbol{q}^\epsilon} = \frac{4\mu}{2-\nu} \left(\frac{1}{2\sqrt{\delta_n^\epsilon}} \frac{\partial \delta_n^\epsilon}{\partial \boldsymbol{q}^\epsilon} + \sqrt{\delta_n^\epsilon} \frac{\partial \delta_t^\epsilon}{\partial \boldsymbol{q}^\epsilon} \right) \ , \ \frac{\partial \delta_t^\epsilon}{\partial \boldsymbol{q}^\epsilon} = \begin{bmatrix} 0 & 1 & 1 & 0 & -1 & 1 \end{bmatrix} \qquad (64)$$

$$\frac{\partial f_\omega^\epsilon}{\partial \boldsymbol{q}^\epsilon} = B \frac{4\mu}{2-\nu} R^{5/2} \frac{\partial (\omega^\alpha + \omega^\beta)}{\partial \boldsymbol{q}^\epsilon} + R \frac{\partial f_y^\epsilon}{\partial \boldsymbol{q}^\epsilon} \ , \ \frac{\partial (\omega^\alpha + \omega^\beta)}{\partial \boldsymbol{q}^\epsilon} = \begin{bmatrix} 0 & 0 & 1 & 0 & 0 & 1 \end{bmatrix} \qquad (65)$$

where the contact moment f_ω^ϵ is calculated by factoring a rotational stiffness with dimensionless scalar B, such that

$$f_\omega^\epsilon = B\frac{4\mu}{2-\nu}R^{5/2}(\omega^\alpha + \omega^\beta) + Rf_y^\epsilon \tag{66}$$

This is done to avoid a rank deficient local consistent tangent $\partial \boldsymbol{f}^{INT,\epsilon}/\partial \boldsymbol{q}^\epsilon$ because of the linear dependence of Rf_y^ϵ on f_y^ϵ.

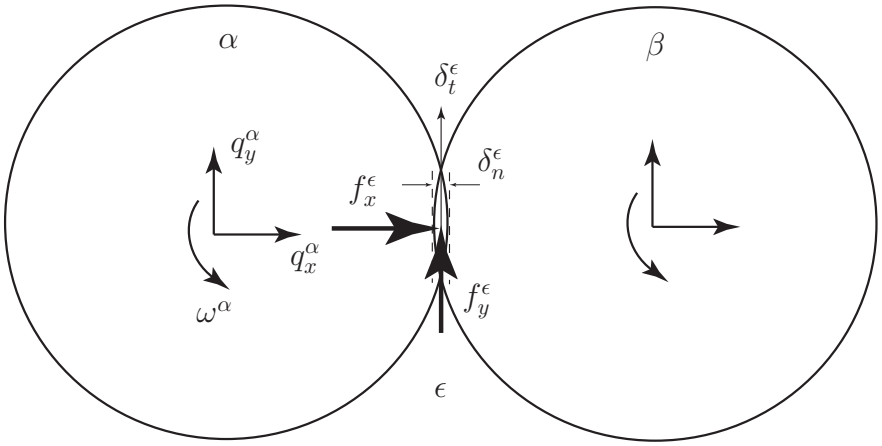

Figure 5. Kinematics and forces of two DE spheres α and β contacting at contact ϵ.

These internal force and moment vectors are assembled into a global nonlinear internal force and moment vector $\boldsymbol{F}^{INT}(\boldsymbol{q})$, that when combined with an external force and moment vector $\boldsymbol{F}^{EXT}$, lead to a residual form of the balance of linear and angular momentum to solve using the Newton-Raphson method,

$$\begin{aligned} \boldsymbol{R}(\boldsymbol{q}) &= \boldsymbol{F}^{INT}(\boldsymbol{q}) - \boldsymbol{F}^{EXT} = \boldsymbol{0} \\ \boldsymbol{F}^{INT}(\boldsymbol{q}) &= \mathop{\mathbf{A}}_{\epsilon=1}^{n_{\text{contacts}}} \boldsymbol{f}^{INT,\epsilon} \end{aligned} \tag{67}$$

For the external force and moment vector $\boldsymbol{F}^{EXT}$, we will insert the boundary conditions directly into the corresponding global dofs in $\boldsymbol{F}^{EXT}$. Simulations using the DE implementation will be demonstrated in the context of the overlap coupling methodology discussed in the next section.

2.4 Overlap Coupling Between 1D Micropolar FEs and a String of Spherical DEs

An aspect of the computational concurrent multiscale modeling approach is to couple regions of material represented by particles, Discrete Element (DE), to regions of material represented by continuum, Finite Element (FE). Another aspect is to bridge the particle mechanics to a continuum representation using finite strain micromorphic elasto-plasticity, whereas the small strain micropolar continuum is a simple approximation of stiff particles with small frictional sliding in the overlap region (we consider no sliding in the numerical examples in sections 2.4.3 and 2.4.4). The coupling implementation will allow arbitrarily overlapping particle and continuum regions in a single "hand-shaking" or overlap region, such that fictitious forces and wave reflections are minimized in the overlap region. In theory, for nearly homogeneous deformation, if the particle and continuum regions share the same region (i.e., are completely overlapped), the results should be the same as if the overlap region is a subset of the overall problem domain (cf. figure 6). This will serve as a benchmark problem for the numerical implementation. The coupling implementation extends to particle mechanics and micropolar continuum the "bridging scale decomposition" proposed by (*19*) and modifications thereof by (*13*) (see references therein for further background on these methods).

2.4.1 3D Kinematics

Here, a summary of the kinematics of the coupled regions is given for general 3-D kinematics, following the illustration shown in figure 6. It is assumed that the finite element mesh covers the domain of the problem in which the material is behaving more solid-like, whereas in regions of large relative particle motion (fluid-like), a particle mechanics representation can be used (in this case, DE). In figure 6, discrete domains are defined, where the purple background denotes the FE overlap region $\tilde{\mathcal{B}}^h$ with underlying ghost particles, aqua blue the FE continuum region $\bar{\mathcal{B}}^h$ with no underlying particles, and white background (with brown particles) the free particle region $\hat{\mathcal{B}}^h \cup \mathcal{B}^{DE}$. In summary, the finite element domain $\mathcal{B}^h$ is the union of pure continuum FE domain $\bar{\mathcal{B}}^h$, overlapping FE domain with underlying ghost particles $\tilde{\mathcal{B}}^h$, and overlapping FE domain with underlying free particles $\hat{\mathcal{B}}^h$, such that $\mathcal{B}^h = \bar{\mathcal{B}}^h \cup \tilde{\mathcal{B}}^h \cup \hat{\mathcal{B}}^h$. The pure particle domain with no overlapping FE domain (i.e., the 'open-window') is indicated by $\mathcal{B}^{DE}$. The goal is to have the overlap region $\hat{\mathcal{B}}^h \cup \tilde{\mathcal{B}}^h$ as close to the region of interest (e.g., penetrator skin) as to minimize the number of particles, and, thus, computational effort. Following some of the same notation presented in (*13*), we define a generalized dof vector $\breve{\boldsymbol{Q}}$ for particle displacements and rotations in the system as

$$\breve{\boldsymbol{Q}} = [\boldsymbol{q}_\alpha, \boldsymbol{q}_\beta, \ldots, \boldsymbol{q}_\gamma, \boldsymbol{\omega}_\alpha, \boldsymbol{\omega}_\beta, \ldots, \boldsymbol{\omega}_\gamma]^T,\ \alpha, \beta, \ldots, \gamma \in \breve{\mathcal{A}} \tag{68}$$

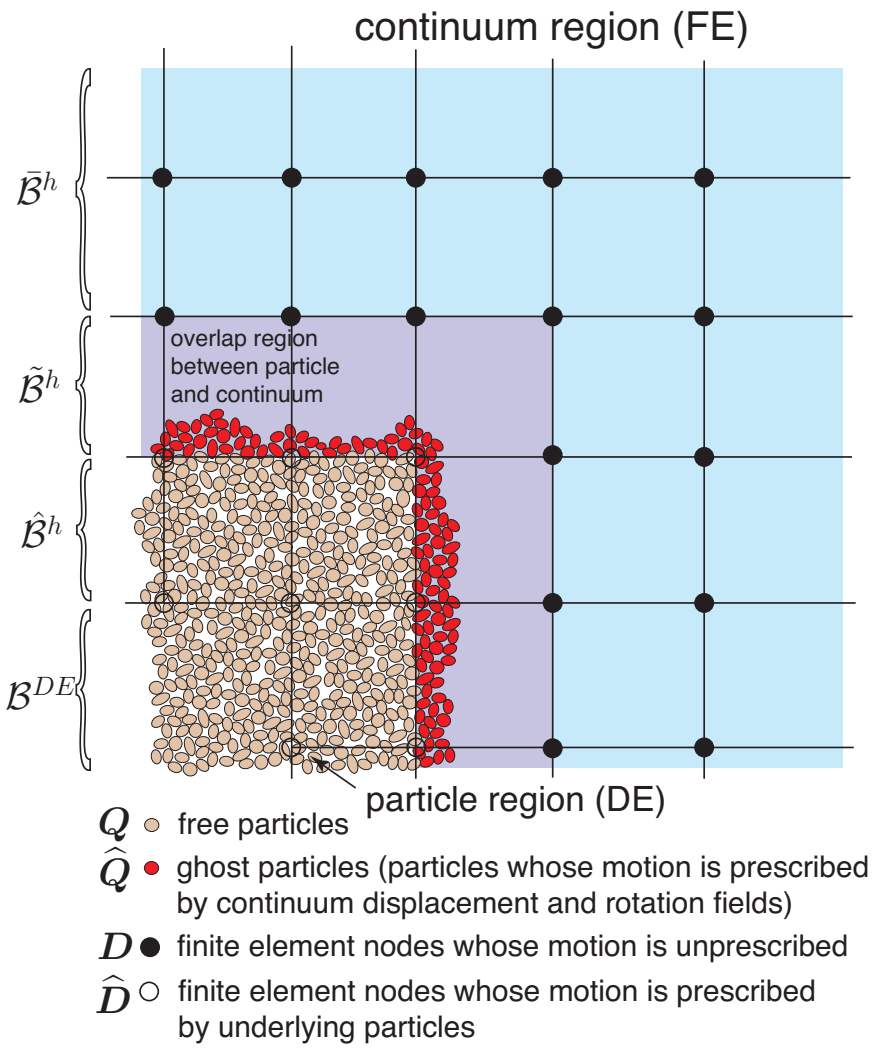

Figure 6. Two-dimensional illustration of the coupling between particle and continuum regions.

where $\boldsymbol{q}_\alpha$ is the displacement vector of particle α, $\boldsymbol{\omega}_\alpha$ its rotation vector, and $\breve{\mathcal{A}}$ is the set of all particles. Likewise, the finite element nodal displacements and rotations are written as

$$\begin{aligned} \breve{\boldsymbol{D}} &= [\boldsymbol{d}_a, \boldsymbol{d}_b, \ldots, \boldsymbol{d}_c, \boldsymbol{\theta}_d, \boldsymbol{\theta}_e, \ldots, \boldsymbol{\theta}_f]^T \\ & \quad a, b, \ldots, c \in \breve{\mathcal{N}}\,, \quad d, e, \ldots, f \in \breve{\mathcal{M}} \end{aligned} \tag{69}$$

where $\boldsymbol{d}_a$ is the displacement vector of node a, $\boldsymbol{\theta}_d$ is the rotation vector of node d, $\breve{\mathcal{N}}$ is the set of all nodes, and $\breve{\mathcal{M}}$ is the set of finite element nodes with rotational degrees of freedom, where $\breve{\mathcal{M}} \subset \breve{\mathcal{N}}$. In order to satisfy the boundary conditions for both regions, the motion of the particles

in the overlap region (referred to as "ghost particles," cf. figure 6) is prescribed by the continuum displacement and rotation fields, and written as

$$\widehat{\boldsymbol{Q}} = [\boldsymbol{q}_\alpha, \boldsymbol{q}_\beta, \ldots, \boldsymbol{q}_\gamma, \boldsymbol{\omega}_\alpha, \boldsymbol{\omega}_\beta, \ldots, \boldsymbol{\omega}_\gamma]^T,\ \alpha, \beta, \ldots, \gamma \in \widehat{\mathcal{A}}\,,\ \widehat{\mathcal{A}} \in \tilde{\mathcal{B}}^h \tag{70}$$

while the unprescribed (or free) particle displacements and rotations are

$$\boldsymbol{Q} = [\boldsymbol{q}_\delta, \boldsymbol{q}_\epsilon, \ldots, \boldsymbol{q}_\eta, \boldsymbol{\omega}_\delta, \boldsymbol{\omega}_\epsilon, \ldots, \boldsymbol{\omega}_\eta]^T\,, \quad \delta, \epsilon, \ldots, \eta \in \mathcal{A}\,,\ \mathcal{A} \in \hat{\mathcal{B}}^h \cup \mathcal{B}^{DE} \tag{71}$$

where $\widehat{\mathcal{A}} \cup \mathcal{A} = \breve{\mathcal{A}}$ and $\widehat{\mathcal{A}} \cap \mathcal{A} = \emptyset$. Likewise, the displacements and rotations of nodes overlaying the particle region are prescribed by the particle motion and written as

$$\begin{aligned} \widehat{\boldsymbol{D}} \;\; = \;\; & [\boldsymbol{d}_a, \boldsymbol{d}_b, \ldots, \boldsymbol{d}_c, \boldsymbol{\theta}_d, \boldsymbol{\theta}_e, \ldots, \boldsymbol{\theta}_f]^T \\ & a, b, \ldots, c \in \widehat{\mathcal{N}}\,, \quad d, e, \ldots, f \in \widehat{\mathcal{M}} \\ & \widehat{\mathcal{N}}, \widehat{\mathcal{M}} \in \tilde{\mathcal{B}}^h \cup \hat{\mathcal{B}}^h \end{aligned} \tag{72}$$

while the unprescribed (or free) nodal displacements and rotations are

$$\begin{aligned} \boldsymbol{D} \;\; = \;\; & [\boldsymbol{d}_m, \boldsymbol{d}_n, \ldots, \boldsymbol{d}_s, \boldsymbol{\theta}_t, \boldsymbol{\theta}_u, \ldots, \boldsymbol{\theta}_v]^T \\ & m, n, \ldots, s \in \mathcal{N}\,, \quad t, u, \ldots, v \in \mathcal{M} \\ & \mathcal{N}, \mathcal{M} \in \tilde{\mathcal{B}}^h \cup \bar{\mathcal{B}}^h \end{aligned} \tag{73}$$

where $\widehat{\mathcal{N}} \cup \mathcal{N} = \breve{\mathcal{N}}$, $\widehat{\mathcal{N}} \cap \mathcal{N} = \emptyset$, $\widehat{\mathcal{M}} \cup \mathcal{M} = \breve{\mathcal{M}}$, and $\widehat{\mathcal{M}} \cap \mathcal{M} = \emptyset$. Referring to figure 6, the prescribed particle motions $\widehat{\boldsymbol{Q}}$ can be viewed as boundary constraints on the free particle region, and likewise the prescribed finite element nodal displacements and rotations $\widehat{\boldsymbol{D}}$ can be viewed as boundary constraints on the finite element mesh in the overlap region.

In general, the displacement vector of a particle α can be represented by the finite element interpolation of the continuum macro-displacement field $\boldsymbol{u}^h$ evaluated at the particle centroid $\boldsymbol{x}_\alpha$, such that

$$\boldsymbol{u}^h(\boldsymbol{x}_\alpha, t) = \sum_{a \in \breve{\mathcal{N}}} N_a^u(\boldsymbol{x}_\alpha) \boldsymbol{d}_a(t)\,, \quad \alpha \in \breve{\mathcal{A}} \tag{74}$$

where N_a^u are the shape functions associated with the continuum displacement field $\boldsymbol{u}^h$. Recall that N_a^u have compact support and, thus, are only evaluated for particles with centroids that lie within an element containing node a in its domain. In DE, particle dofs (translations and rotations) are tracked at the particle centroids, as are resultant forces and moments (from forces acting at contacts). For example, we can write the prescribed displacement of ghost particle α as

$$\boldsymbol{q}_\alpha(t) = \boldsymbol{u}^h(\boldsymbol{x}_\alpha, t) = \sum_{a \in \check{\mathcal{N}}} N_a^u(\boldsymbol{x}_\alpha)\boldsymbol{d}_a(t) \ , \quad \alpha \in \widehat{\mathcal{A}} \tag{75}$$

Likewise, particle rotation vectors can be represented by the finite element interpolation of the continuum micro-rotation field $\boldsymbol{\varphi}^h$ evaluated at the particle centroid $\boldsymbol{x}_\alpha$, such that

$$\boldsymbol{\varphi}^h(\boldsymbol{x}_\alpha, t) = \sum_{b \in \check{\mathcal{M}}} N_b^\varphi(\boldsymbol{x}_\alpha)\boldsymbol{\theta}_b(t) \ , \quad \alpha \in \check{\mathcal{A}} \tag{76}$$

where N_b^φ are the shape functions associated with the micro-rotation field $\boldsymbol{\varphi}^h$. For example, we can write the prescribed rotation of ghost particle α as

$$\boldsymbol{\omega}_\alpha(t) = \boldsymbol{\varphi}^h(\boldsymbol{x}_\alpha, t) = \sum_{b \in \check{\mathcal{M}}} N_b^\varphi(\boldsymbol{x}_\alpha)\boldsymbol{\theta}_b(t) \ , \quad \alpha \in \widehat{\mathcal{A}} \tag{77}$$

For all ghost particles (cf. figure 6), the interpolations can be written as

$$\widehat{\boldsymbol{Q}} = \boldsymbol{N}_{\widehat{Q}D} \cdot \boldsymbol{D} + \boldsymbol{N}_{\widehat{Q}\widehat{D}} \cdot \widehat{\boldsymbol{D}} \tag{78}$$

where $\boldsymbol{N}_{\widehat{Q}D}$ and $\boldsymbol{N}_{\widehat{Q}\widehat{D}}$ are shape function matrices containing individual nodal shape functions N_a^u and N_b^φ, but for now these matrices will be kept general to increase our flexibility in choosing interpolation/projection functions (such as those used in meshfree methods). Overall, the particle displacements and rotations may be written as

$$\begin{bmatrix} \boldsymbol{Q} \\ \widehat{\boldsymbol{Q}} \end{bmatrix} = \begin{bmatrix} \boldsymbol{N}_{QD} & \boldsymbol{N}_{Q\widehat{D}} \\ \boldsymbol{N}_{\widehat{Q}D} & \boldsymbol{N}_{\widehat{Q}\widehat{D}} \end{bmatrix} \cdot \begin{bmatrix} \boldsymbol{D} \\ \widehat{\boldsymbol{D}} \end{bmatrix} + \begin{bmatrix} \boldsymbol{Q}' \\ \boldsymbol{0} \end{bmatrix} \tag{79}$$

where $\boldsymbol{Q}'$ is introduced (*13*) as the error (or "fine-scale" (*19*)) in the interpolation of the free particle displacements and rotations $\boldsymbol{Q}$, whose function space is not rich enough to represent the true free particle motion. The shape function matrices $\boldsymbol{N}$ are, in general, not square because the

number of free particles are not the same as free nodes and prescribed nodes, and the number of ghost particles is not the same as prescribed and free nodes. A scalar measure of error in particle displacements and rotations is defined as (*13*)

$$e = \boldsymbol{Q}' \cdot \boldsymbol{Q}' \tag{80}$$

which may be minimized with respect to prescribed continuum nodal dofs $\widehat{\boldsymbol{D}}$ to solve for $\widehat{\boldsymbol{D}}$ in terms of free particle and continuum nodal dofs as

$$\widehat{\boldsymbol{D}} = \boldsymbol{M}^{-1}_{\widehat{D}\widehat{D}} \boldsymbol{N}^{T}_{Q\widehat{D}} (\boldsymbol{Q} - \boldsymbol{N}_{QD} \boldsymbol{D}) \ , \quad \boldsymbol{M}_{\widehat{D}\widehat{D}} = \boldsymbol{N}^{T}_{Q\widehat{D}} \boldsymbol{N}_{Q\widehat{D}} \tag{81}$$

This is known as the "discretized L_2 projection" (*13*) of the free particle motion $\boldsymbol{Q}$ and free nodal dofs $\boldsymbol{D}$ onto the prescribed nodals dofs $\widehat{\boldsymbol{D}}$. Upon substituting equation 81 into equation 78, we may write the prescribed particle dofs $\widehat{\boldsymbol{Q}}$ in terms of free particle $\boldsymbol{Q}$ and continuum nodal $\boldsymbol{D}$ dofs. In summary, these relations are written as

$$\widehat{\boldsymbol{Q}} = \boldsymbol{B}_{\widehat{Q}Q} \boldsymbol{Q} + \boldsymbol{B}_{\widehat{Q}D} \boldsymbol{D} \tag{82}$$

$$\widehat{\boldsymbol{D}} = \boldsymbol{B}_{\widehat{D}Q} \boldsymbol{Q} + \boldsymbol{B}_{\widehat{D}D} \boldsymbol{D} \tag{83}$$

where

$$\boldsymbol{B}_{\widehat{Q}Q} = \boldsymbol{N}_{\widehat{Q}\widehat{D}} \boldsymbol{B}_{\widehat{D}Q} \tag{84}$$

$$\boldsymbol{B}_{\widehat{Q}D} = \boldsymbol{N}_{\widehat{Q}D} + \boldsymbol{N}_{\widehat{Q}\widehat{D}} \boldsymbol{B}_{\widehat{D}D} \tag{85}$$

$$\boldsymbol{B}_{\widehat{D}Q} = \boldsymbol{M}^{-1}_{\widehat{D}\widehat{D}} \boldsymbol{N}^{T}_{Q\widehat{D}} \tag{86}$$

$$\boldsymbol{B}_{\widehat{D}D} = -\boldsymbol{M}^{-1}_{\widehat{D}\widehat{D}} \boldsymbol{N}^{T}_{Q\widehat{D}} \boldsymbol{N}_{QD} \tag{87}$$

As shown in figure 6, for a finite element implementation of this dof coupling, we expect that free particle dofs $\boldsymbol{Q}$ will not fall within the support of free continuum nodal dofs $\boldsymbol{D}$, such that it can be assumed that $\boldsymbol{N}_{QD} = \boldsymbol{0}$ and

$$\widehat{\boldsymbol{Q}} = \boldsymbol{B}_{\widehat{Q}Q} \boldsymbol{Q} + \boldsymbol{B}_{\widehat{Q}D} \boldsymbol{D} \ , \ \widehat{\boldsymbol{D}} = \boldsymbol{B}_{\widehat{D}Q} \boldsymbol{Q} \tag{88}$$

where

$$\boldsymbol{B}_{\widehat{Q}Q} = \boldsymbol{N}_{\widehat{Q}\widehat{D}}\boldsymbol{B}_{\widehat{D}Q} \ , \ \boldsymbol{B}_{\widehat{Q}D} = \boldsymbol{N}_{\widehat{Q}D} \tag{89}$$

$$\boldsymbol{B}_{\widehat{D}Q} = \boldsymbol{M}^{-1}_{\widehat{D}\widehat{D}}\boldsymbol{N}^{T}_{Q\widehat{D}} \ , \ \boldsymbol{B}_{\widehat{D}D} = \boldsymbol{0} \tag{90}$$

The assumption $\boldsymbol{N}_{QD} \neq \boldsymbol{0}$ would be valid for a meshfree projection of the particle motions to the FE nodal dofs, as in (*13*), where we could imagine that the domain of influence of the meshfree projection could encompass a free particle centroid; the degree of encompassment would be controlled by the chosen support size of the meshfree kernel function. The choice of meshfree projection in (*13*) was not necessarily to allow $\boldsymbol{Q}$ be projected to $\boldsymbol{D}$ (and vice versa), but to remove the computationally costly calculation of the inverse $\boldsymbol{M}^{-1}_{\widehat{D}\widehat{D}}$ in equations 82 and 83.

2.4.2 3D Kinetic and Potential Energy Partitioning and Coupling

For the particle DE equations, the kinetic energy is T^Q, dissipation function F^Q, and potential energy U^Q, such that

$$\begin{aligned} T^Q &= \frac{1}{2}\dot{\boldsymbol{Q}}\boldsymbol{M}^Q\dot{\boldsymbol{Q}} \\ F^Q &= aT^Q \\ U^Q(\boldsymbol{Q}) &= \int_{\boldsymbol{0}}^{\boldsymbol{Q}} \boldsymbol{F}^{INT,Q}(\boldsymbol{S})d\boldsymbol{S} \end{aligned} \tag{91}$$

where $\boldsymbol{M}^Q$ is a mass and rotary inertia matrix (not given in section 2.3), and $\boldsymbol{F}^{INT,Q}$ is provided from equation 67. The dissipation function F^Q is written as a linear function of the kinetic energy T^Q with proportionality coefficient a, which falls within the class of damping called "Rayleigh damping" (pg.130 of (*20*)). For the micropolar continuum FE equations, T^D is the kinetic energy, F^D the dissipation function, and U^D the potential energy, such that

$$\begin{aligned} T^D &= \frac{1}{2}\dot{\boldsymbol{D}}\boldsymbol{M}^D\dot{\boldsymbol{D}} \\ F^D &= 0 \\ U^D(\boldsymbol{D}) &= \int_{\boldsymbol{0}}^{\boldsymbol{D}} \boldsymbol{F}^{INT,D}(\boldsymbol{S})d\boldsymbol{S} \end{aligned} \tag{92}$$

where $\boldsymbol{M}^D$ and $\boldsymbol{F}^{INT,D}(\boldsymbol{S}) = \boldsymbol{K}^D\boldsymbol{S}$ come from equation 51. We assume the total kinetic and potential energy and dissipation of the coupled particle-continuum system may be written as the sum of the energies

$$
\begin{aligned}
T(\dot{\boldsymbol{Q}},\dot{\boldsymbol{D}}) &= T^Q(\dot{\boldsymbol{Q}},\dot{\widehat{\boldsymbol{Q}}}(\dot{\boldsymbol{Q}},\dot{\boldsymbol{D}})) + T^D(\dot{\boldsymbol{D}},\dot{\widehat{\boldsymbol{D}}}(\dot{\boldsymbol{Q}})) && (93)\\
U(\boldsymbol{Q},\boldsymbol{D}) &= U^Q(\boldsymbol{Q},\widehat{\boldsymbol{Q}}(\boldsymbol{Q},\boldsymbol{D})) + U^D(\boldsymbol{D},\widehat{\boldsymbol{D}}(\boldsymbol{Q})) && (94)\\
F(\dot{\boldsymbol{Q}},\dot{\boldsymbol{D}}) &= F^Q(\dot{\boldsymbol{Q}},\dot{\widehat{\boldsymbol{Q}}}(\dot{\boldsymbol{Q}},\dot{\boldsymbol{D}})) && (95)
\end{aligned}
$$

where we have indicated the functional dependence of the prescribed particle motion and nodal dofs solely upon the free particle motion and nodal dofs $\boldsymbol{Q}$ and $\boldsymbol{D}$, respectively. Note that the dissipation function $F = F^Q$ only applies for the particle system, and only for static problems (dynamic relaxation DE simulation). For purely dynamical problems, $F^Q = 0$, and there is only dissipation in the particle system if particles are allowed to slide frictionally, and the continuum has plasticity or other inelastic constitutive response. Lagrange's equations may then be stated as

$$
\begin{aligned}
\frac{d}{dt}\left(\frac{\partial T}{\partial \dot{\boldsymbol{Q}}}\right) - \frac{\partial T}{\partial \boldsymbol{Q}} + \frac{\partial F}{\partial \dot{\boldsymbol{Q}}} + \frac{\partial U}{\partial \boldsymbol{Q}} &= \boldsymbol{F}^{EXT,Q}\\
\frac{d}{dt}\left(\frac{\partial T}{\partial \dot{\boldsymbol{D}}}\right) - \frac{\partial T}{\partial \boldsymbol{D}} + \frac{\partial F}{\partial \dot{\boldsymbol{D}}} + \frac{\partial U}{\partial \boldsymbol{D}} &= \boldsymbol{F}^{EXT,D} && (96)
\end{aligned}
$$

which lead to a coupled system of governing equations (linear and angular momentum) for the coupled particle-continuum mechanics. The derivatives are

$$
\begin{aligned}
\frac{\partial T}{\partial \dot{\boldsymbol{Q}}} &= \frac{\partial T^Q}{\partial \dot{\boldsymbol{Q}}} + \frac{\partial T^Q}{\partial \dot{\widehat{\boldsymbol{Q}}}}\boldsymbol{B}_{\widehat{Q}Q} + \frac{\partial T^D}{\partial \dot{\widehat{\boldsymbol{D}}}}\boldsymbol{B}_{\widehat{D}Q}\ ,\ \frac{\partial T}{\partial \boldsymbol{Q}} = \boldsymbol{0} && (97)\\
\frac{\partial F}{\partial \dot{\boldsymbol{Q}}} &= \frac{\partial F^Q}{\partial \dot{\boldsymbol{Q}}} = a\left(\frac{\partial T^Q}{\partial \dot{\boldsymbol{Q}}} + \frac{\partial T^Q}{\partial \dot{\widehat{\boldsymbol{Q}}}}\boldsymbol{B}_{\widehat{Q}Q}\right) && (98)\\
\frac{\partial U}{\partial \boldsymbol{Q}} &= \frac{\partial U^Q}{\partial \boldsymbol{Q}} + \frac{\partial U^Q}{\partial \widehat{\boldsymbol{Q}}}\boldsymbol{B}_{\widehat{Q}Q} + \frac{\partial U^D}{\partial \widehat{\boldsymbol{D}}}\boldsymbol{B}_{\widehat{D}Q} && (99)\\
\frac{\partial T}{\partial \dot{\boldsymbol{D}}} &= \frac{\partial T^D}{\partial \dot{\boldsymbol{D}}} + \frac{\partial T^D}{\partial \dot{\widehat{\boldsymbol{D}}}}\boldsymbol{B}_{\widehat{D}D} + \frac{\partial T^Q}{\partial \dot{\widehat{\boldsymbol{Q}}}}\boldsymbol{B}_{\widehat{Q}D} && (100)\\
\frac{\partial T}{\partial \boldsymbol{D}} &= \boldsymbol{0}\ ,\ \frac{\partial F}{\partial \dot{\boldsymbol{D}}} = \boldsymbol{0} && (101)\\
\frac{\partial U}{\partial \boldsymbol{D}} &= \frac{\partial U^D}{\partial \boldsymbol{D}} + \frac{\partial U^D}{\partial \widehat{\boldsymbol{D}}}\boldsymbol{B}_{\widehat{D}D} + \frac{\partial U^Q}{\partial \widehat{\boldsymbol{Q}}}\boldsymbol{B}_{\widehat{Q}D} && (102)
\end{aligned}
$$

If the potential energy U is nonlinear with regard to particle frictional sliding and micropolar (or micromorphic) plasticity, then (96) may be integrated in time and linearized for solution by the Newton-Raphson method. The benefit of this multiscale method, as pointed out by (*19*), is that time steps are different for the DE and FE solutions. A multiscale time stepping scheme will follow an approach similar to (*19*). To complete (96) and identify an approach to energy partitioning, the individual derivatives may be written as

$$\frac{\partial T^Q}{\partial \dot{\boldsymbol{Q}}} = \boldsymbol{M}^Q \dot{\boldsymbol{Q}} \ , \ \frac{\partial T^Q}{\partial \dot{\widehat{\boldsymbol{Q}}}} = \boldsymbol{M}^{\widehat{Q}} \dot{\widehat{\boldsymbol{Q}}} \tag{103}$$

$$\frac{\partial T^D}{\partial \dot{\boldsymbol{D}}} = \boldsymbol{M}^D \dot{\boldsymbol{D}} \ , \ \frac{\partial T^D}{\partial \dot{\widehat{\boldsymbol{D}}}} = \boldsymbol{M}^{\widehat{D}} \dot{\widehat{\boldsymbol{D}}} \tag{104}$$

$$\frac{\partial F}{\partial \dot{\boldsymbol{Q}}} = a \left(\boldsymbol{M}^Q \dot{\boldsymbol{Q}} + \boldsymbol{B}^T_{\widehat{Q}Q} \boldsymbol{M}^{\widehat{Q}} \dot{\widehat{\boldsymbol{Q}}} \right) \tag{105}$$

$$\frac{\partial U^Q}{\partial \boldsymbol{Q}} = \boldsymbol{F}^{INT,Q}(\boldsymbol{Q}) \ , \ \frac{\partial U^Q}{\partial \widehat{\boldsymbol{Q}}} = \boldsymbol{F}^{INT,\widehat{Q}}(\widehat{\boldsymbol{Q}}) \tag{106}$$

$$\frac{\partial U^D}{\partial \boldsymbol{D}} = \boldsymbol{F}^{INT,D}(\boldsymbol{D}) \ , \ \frac{\partial U^D}{\partial \widehat{\boldsymbol{D}}} = \boldsymbol{F}^{INT,\widehat{D}}(\widehat{\boldsymbol{D}}) \tag{107}$$

where superscript Q denotes free particle motion and $\widehat{Q}$ ghost particle motion, whereas superscript D denotes free nodal dofs and $\widehat{D}$ prescribed nodal dofs. The energy partitioning will be introduced through the definition of these terms below. First, substitute equations 103–107 into equation 96 to arrive at the coupled nonlinear equations in terms of $\boldsymbol{Q}$ and $\boldsymbol{D}$ as

$$\begin{aligned}
&\left(\boldsymbol{M}^Q + \boldsymbol{B}^T_{\widehat{Q}Q} \boldsymbol{M}^{\widehat{Q}} \boldsymbol{B}_{\widehat{Q}Q} + \boldsymbol{B}^T_{\widehat{D}Q} \boldsymbol{M}^{\widehat{D}} \boldsymbol{B}_{\widehat{D}Q} \right) \ddot{\boldsymbol{Q}} \\
&+ \left(\boldsymbol{B}^T_{\widehat{Q}Q} \boldsymbol{M}^{\widehat{Q}} \boldsymbol{B}_{\widehat{Q}D} + \boldsymbol{B}^T_{\widehat{D}Q} \boldsymbol{M}^{\widehat{D}} \boldsymbol{B}_{\widehat{D}D} \right) \ddot{\boldsymbol{D}} \\
&+ \left(\boldsymbol{C}^Q + \boldsymbol{B}^T_{\widehat{Q}Q} \boldsymbol{C}^{\widehat{Q}} \boldsymbol{B}_{\widehat{Q}Q} \right) \dot{\boldsymbol{Q}} + \boldsymbol{B}^T_{\widehat{Q}Q} \boldsymbol{C}^{\widehat{Q}} \boldsymbol{B}_{\widehat{Q}D} \dot{\boldsymbol{D}} \\
&+ \boldsymbol{F}^{INT,Q}(\boldsymbol{Q}) + \boldsymbol{B}^T_{\widehat{Q}Q} \boldsymbol{F}^{INT,\widehat{Q}} [\boldsymbol{B}_{\widehat{Q}Q} \boldsymbol{Q} + \boldsymbol{B}_{\widehat{Q}D} \boldsymbol{D}] \\
&+ \boldsymbol{B}^T_{\widehat{D}Q} \boldsymbol{F}^{INT,\widehat{D}} [\boldsymbol{B}_{\widehat{D}Q} \boldsymbol{Q} + \boldsymbol{B}_{\widehat{D}D} \boldsymbol{D}] = \boldsymbol{F}^{EXT,Q} + \boldsymbol{B}^T_{\widehat{Q}Q} \boldsymbol{F}^{EXT,\widehat{Q}}
\end{aligned} \tag{108}$$

$$\begin{aligned}
&\left(\boldsymbol{B}^T_{\widehat{Q}D} \boldsymbol{M}^{\widehat{Q}} \boldsymbol{B}_{\widehat{Q}D} + \boldsymbol{B}^T_{\widehat{D}D} \boldsymbol{M}^{\widehat{D}} \boldsymbol{B}_{\widehat{D}Q} \right) \ddot{\boldsymbol{Q}} \\
&+ \left(\boldsymbol{M}^D + \boldsymbol{B}^T_{\widehat{Q}D} \boldsymbol{M}^{\widehat{Q}} \boldsymbol{B}_{\widehat{Q}D} + \boldsymbol{B}^T_{\widehat{D}D} \boldsymbol{M}^{\widehat{D}} \boldsymbol{B}_{\widehat{D}D} \right) \ddot{\boldsymbol{D}} \\
&+ \boldsymbol{B}^T_{\widehat{Q}D} \boldsymbol{F}^{INT,\widehat{Q}} [\boldsymbol{B}_{\widehat{Q}Q} \boldsymbol{Q} + \boldsymbol{B}_{\widehat{Q}D} \boldsymbol{D}] + \boldsymbol{B}^T_{\widehat{D}D} \boldsymbol{F}^{INT,\widehat{D}} [\boldsymbol{B}_{\widehat{D}Q} \boldsymbol{Q} + \boldsymbol{B}_{\widehat{D}D} \boldsymbol{D}] \\
&+ \boldsymbol{F}^{INT,D}(\boldsymbol{D}) = \boldsymbol{F}^{EXT,D} + \boldsymbol{B}^T_{\widehat{D}D} \boldsymbol{F}^{EXT,\widehat{D}}
\end{aligned} \tag{109}$$

where an expression in brackets $[\bullet]$ denotes the functional dependence of the nonlinear internal force and moment vector. Note the projections through the $\boldsymbol{B}$ matrices of the corresponding mass, rotary inertia, and damping matrices, and forcing and moment vectors. First, starting with the mass and rotary inertia matrices for the particles, we partition the kinetic energy[5] as follows:

$$\boldsymbol{M}^{\widehat{Q}} = (1-\hat{r}) \mathop{\mathbf{A}}_{\alpha} \boldsymbol{m}_{\alpha}^{Q} \ , \ \alpha \in \hat{\mathcal{A}} \ , \ \boldsymbol{x}_{\alpha} \in \tilde{\mathcal{B}}^{h} \tag{110}$$

$$\boldsymbol{M}^{Q} = \boldsymbol{M}^{DE,Q} + \widehat{\boldsymbol{M}}^{Q} \tag{111}$$

$$\boldsymbol{M}^{DE,Q} = \mathop{\mathbf{A}}_{\beta} \boldsymbol{m}_{\beta}^{Q} \ , \ \beta \in \mathcal{A} \ , \ \boldsymbol{x}_{\beta} \in \mathcal{B}^{DE}$$

$$\widehat{\boldsymbol{M}}^{Q} = (1-\hat{r}) \mathop{\mathbf{A}}_{\beta} \boldsymbol{m}_{\beta}^{Q} \ , \ \beta \in \mathcal{A} \ , \ \boldsymbol{x}_{\beta} \in \hat{\mathcal{B}}^{h}$$

where $\boldsymbol{M}^{\widehat{Q}}$ is the mass and rotary inertia matrix of ghost particles in $\tilde{\mathcal{B}}^{h}$, $\boldsymbol{M}^{DE,Q}$ the mass and rotary inertia matrix of free particles in $\mathcal{B}^{DE}$, $\widehat{\boldsymbol{M}}^{Q}$ the mass and rotary inertia matrix of free particles in $\hat{\mathcal{B}}^{h}$, and $\hat{r}$ is a weighting factor for the kinetic energy in the overlap region $\hat{\mathcal{B}}^{h} \cup \tilde{\mathcal{B}}^{h}$. For no homogenized continuum contribution to the kinetic energy in the overlap region, $\hat{r} = 0$, and for full continuum homogenization of the underlying particle kinetic energy, $\hat{r} = 1$. In our case, we will consider the range $0 \leq \hat{r} \leq 1$. Given that the proposed multiscale modeling framework is to be used in an adaptive fashion in the future, having an overlaying continuum homogenization of the particle response is attractive when particle is converted to continuum representation, and vice versa (in a statistical manner[6]). For the mass and rotary inertia matrices associated with the micropolar continuum, we partition the kinetic energy as follows:

[5] and dissipation function through the mass-proportional damping for dynamic relaxation of a static DE analysis

[6] statistical, in the sense of generating a particle representation from a continuum one, where the underlying particle system does not exist; converting from particle to continuum representation is straightforward given the built-in homogenization that the micropolar continuum possesses

$$
\begin{aligned}
\boldsymbol{M}^{\widehat{D}} &= \widetilde{\boldsymbol{M}}^{\widehat{D}} + \widehat{\boldsymbol{M}}^{\widehat{D}} \qquad (112)\\
&\widetilde{\boldsymbol{M}}^{\breve{D}} = \begin{bmatrix} \widetilde{\boldsymbol{M}}^{\breve{u}} & \mathbf{0} \\ \mathbf{0} & \widetilde{\boldsymbol{M}}^{\breve{\varphi}} \end{bmatrix}\\
&\widetilde{\boldsymbol{M}}^{\breve{u}} = \mathop{\mathsf{A}}_{e\in\tilde{\mathcal{B}}^h} \left(\hat{r}\,\langle \boldsymbol{m}^{u,e}\rangle + \tilde{r}^e \boldsymbol{m}^{u,e}\right)\\
&\widetilde{\boldsymbol{M}}^{\breve{\varphi}} = \mathop{\mathsf{A}}_{e\in\tilde{\mathcal{B}}^h} \left(\hat{r}\,\langle \boldsymbol{m}^{\varphi,e}\rangle + \tilde{r}^e \boldsymbol{m}^{\varphi,e}\right)\\
&\widehat{\boldsymbol{M}}^{\widehat{D}} = \hat{r}\begin{bmatrix} \widehat{\boldsymbol{M}}^{\hat{u}} & \mathbf{0} \\ \mathbf{0} & \widehat{\boldsymbol{M}}^{\hat{\varphi}} \end{bmatrix}, \quad \widehat{\boldsymbol{M}}^{\hat{u}} = \mathop{\mathsf{A}}_{e\in\hat{\mathcal{B}}^h} \langle \boldsymbol{m}^{u,e}\rangle \;,\; \widehat{\boldsymbol{M}}^{\hat{\varphi}} = \mathop{\mathsf{A}}_{e\in\hat{\mathcal{B}}^h} \langle \boldsymbol{m}^{\varphi,e}\rangle\\
\boldsymbol{M}^{D} &= \widetilde{\boldsymbol{M}}^{D} + \bar{\boldsymbol{M}}^{D} \qquad (113)\\
&\bar{\boldsymbol{M}}^{D} = \begin{bmatrix} \bar{\boldsymbol{M}}^{u} & \mathbf{0} \\ \mathbf{0} & \bar{\boldsymbol{M}}^{\varphi} \end{bmatrix}, \quad \bar{\boldsymbol{M}}^{u} = \mathop{\mathsf{A}}_{e\in\bar{\mathcal{B}}^h} \boldsymbol{m}^{u,e} \;,\; \bar{\boldsymbol{M}}^{\varphi} = \mathop{\mathsf{A}}_{e\in\bar{\mathcal{B}}^h} \boldsymbol{m}^{\varphi,e}
\end{aligned}
$$

where $\widetilde{\boldsymbol{M}}^{\widehat{D}}$ is the continuum mass and rotary inertia matrix associated with prescribed nodal dofs in $\tilde{\mathcal{B}}^h$, $\widetilde{\boldsymbol{M}}^{D}$ the continuum mass and rotary inertia matrix associated with free nodal dofs in $\tilde{\mathcal{B}}^h$, where $\widetilde{\boldsymbol{M}}^{\widehat{D}}$ and $\widetilde{\boldsymbol{M}}^{D}$ are extracted from the total mass and rotary inertia matrix $\widetilde{\boldsymbol{M}}^{\breve{D}}$ in $\tilde{\mathcal{B}}^h$, with superscript $(\bullet)^{\breve{D}}$ denoting the full mass and rotary inertia matrix associated with elements in $\tilde{\mathcal{B}}^h$, $\langle\bullet\rangle$ is a homogenization operator, $\tilde{r}^e$ is the partitioning coefficient of continuum kinetic energy associated with element $\mathcal{B}^e \subset \tilde{\mathcal{B}}^h$. A simple choice is a volume fraction $\tilde{r}^e = \mathcal{B}^{e,D}/\mathcal{B}^e$, where $\mathcal{B}^{e,D} = \mathcal{B}^e - \mathcal{B}^{e,\widehat{Q}}$; $\mathcal{B}^{e,D}$ is the non-overlapping continuum part of element volume $\mathcal{B}^e \subset \tilde{\mathcal{B}}^h$, and $\mathcal{B}^{e,\widehat{Q}}$ is the overlapped ghost particle volume in the element (cf. figure 6). For kinetic energy partitioning, a volume fraction that directly relates to mass and rotary inertia partitioning seems an appropriate choice. $\widehat{\boldsymbol{M}}^{\widehat{D}}$ is the homogenized continuum mass and rotary inertia matrix associated with prescribed nodal dofs in $\hat{\mathcal{B}}^h$; where if $\hat{r} = 0$, there is no continuum homogenization in $\hat{\mathcal{B}}^h$ (i.e., all kinetic energy is due to underlying particles). $\bar{\boldsymbol{M}}^{D}$ is the continuum mass and rotary inertia matrix associated with free nodal dofs in the pure continuum FE domain $\bar{\mathcal{B}}^h$.

For the potential energy (internal force and moment) and external force partitioning in the particle system, we write

$$\boldsymbol{F}^{INT,\widehat{Q}} = (1-\hat{q}) \mathop{\mathsf{A}}_{\epsilon} \boldsymbol{f}_{\epsilon}^{INT,Q} \ , \ \boldsymbol{x}_{\epsilon} \in \tilde{\mathcal{B}}^{h} \tag{114}$$

$$\begin{aligned} \boldsymbol{F}^{INT,Q} &= \boldsymbol{F}^{INT,DE,Q} + \widehat{\boldsymbol{F}}^{INT,Q} \\ \boldsymbol{F}^{INT,DE,Q} &= \mathop{\mathsf{A}}_{\delta} \boldsymbol{f}_{\delta}^{INT,Q} \ , \ \boldsymbol{x}_{\delta} \in \mathcal{B}^{DE} \\ \widehat{\boldsymbol{F}}^{INT,Q} &= (1-\hat{q}) \mathop{\mathsf{A}}_{\delta} \boldsymbol{f}_{\delta}^{INT,Q} \ , \ \boldsymbol{x}_{\delta} \in \hat{\mathcal{B}}^{h} \end{aligned} \tag{115}$$

$$\boldsymbol{F}^{EXT,\widehat{Q}} = (1-\hat{q}) \mathop{\mathsf{A}}_{\epsilon} \boldsymbol{f}_{\epsilon}^{EXT,Q} \ , \ \boldsymbol{x}_{\epsilon} \in \tilde{\mathcal{B}}^{h} \tag{116}$$

$$\begin{aligned} \boldsymbol{F}^{EXT,Q} &= \boldsymbol{F}^{EXT,DE,Q} + \widehat{\boldsymbol{F}}^{EXT,Q} \\ \boldsymbol{F}^{EXT,DE,Q} &= \mathop{\mathsf{A}}_{\delta} \boldsymbol{f}_{\delta}^{EXT,Q} \ , \ \boldsymbol{x}_{\delta} \in \mathcal{B}^{DE} \\ \widehat{\boldsymbol{F}}^{EXT,Q} &= (1-\hat{q}) \mathop{\mathsf{A}}_{\delta} \boldsymbol{f}_{\delta}^{EXT,Q} \ , \ \boldsymbol{x}_{\delta} \in \hat{\mathcal{B}}^{h} \end{aligned} \tag{117}$$

where $\boldsymbol{F}^{INT,\widehat{Q}}$ is the internal force and moment vector associated with ghost particle contacts in $\tilde{\mathcal{B}}^{h}$, $\boldsymbol{F}^{INT,DE,Q}$ is the internal force and moment vector associated with free particle contacts in $\mathcal{B}^{DE}$, $\widehat{\boldsymbol{F}}^{INT,Q}$ is the internal force and moment vector associated with free particle contacts in $\hat{\mathcal{B}}^{h}$, $\boldsymbol{F}^{EXT,\widehat{Q}}$ is the external force and moment vector associated with ghost particle contacts in $\tilde{\mathcal{B}}^{h}$, $\boldsymbol{F}^{EXT,DE,Q}$ is the external force and moment vector associated with free particle contacts in $\mathcal{B}^{DE}$, $\widehat{\boldsymbol{F}}^{EXT,Q}$ is the external force and moment vector associated with free particle contacts in $\hat{\mathcal{B}}^{h}$, and $\hat{q}$ is a weighting factor for the potential energy in the overlap region $\hat{\mathcal{B}}^{h} \cup \tilde{\mathcal{B}}^{h}$. For no homogenized continuum contribution to the potential energy in the overlap region, $\hat{q} = 0$, and for full continuum homogenization of the underlying particle potential energy, $\hat{q} = 1$. In our case, we will consider the range $0 \leq \hat{q} \leq 1$. Note that in (*13*), they chose $\hat{q} = 0$. Their Cauchy-Born elastic constitutive model acts like a homogenization operator on the underlying atomistic response, but instead of keeping an overlain Cauchy-Born representation, the potential energy is completely represented by the underlying atomistic response, except in the overlap region $\tilde{\mathcal{B}}^{h}$ where partitioning occurs. Note that $\boldsymbol{x}_{\epsilon}$ and $\boldsymbol{x}_{\delta}$ denote positions of particle contacts for calculating internal force and moment vectors in equations 114–118, whereas $\boldsymbol{x}_{\alpha}$ and $\boldsymbol{x}_{\beta}$ in equations 110 and 111 denote particle centroids for calculating particle mass and rotary inertia matrices.

For the potential energy (internal force) partitioning in the continuum, we write

$$\begin{aligned} \boldsymbol{F}^{INT,D} &= \widetilde{\boldsymbol{F}}^{INT,D} + \bar{\boldsymbol{F}}^{INT,D} \\ \bar{\boldsymbol{F}}^{INT,D} &= \begin{bmatrix} \bar{\boldsymbol{F}}^{INT,u} \\ \bar{\boldsymbol{F}}^{INT,\varphi} \end{bmatrix} \\ \bar{\boldsymbol{F}}^{INT,u} &= \mathop{\mathsf{A}}_{e \in \bar{\mathcal{B}}^h} \boldsymbol{f}^{INT,u,e} \ , \ \bar{\boldsymbol{F}}^{INT,\varphi} = \mathop{\mathsf{A}}_{e \in \bar{\mathcal{B}}^h} \boldsymbol{f}^{INT,\varphi,e} \end{aligned} \tag{118}$$

and

$$\begin{aligned} \boldsymbol{F}^{INT,\widehat{D}} &= \widetilde{\boldsymbol{F}}^{INT,\widehat{D}} + \widehat{\boldsymbol{F}}^{INT,\widehat{D}} \\ \widetilde{\boldsymbol{F}}^{INT,\breve{D}} &= \begin{bmatrix} \widetilde{\boldsymbol{F}}^{INT,\breve{u}} \\ \widetilde{\boldsymbol{F}}^{INT,\breve{\varphi}} \end{bmatrix} \\ \widetilde{\boldsymbol{F}}^{INT,\breve{u}} &= \mathop{\mathsf{A}}_{e \in \tilde{\mathcal{B}}^h} \left(\hat{q} \left\langle \boldsymbol{f}^{INT,u,e} \right\rangle + \tilde{q}^e \boldsymbol{f}^{INT,u,e} \right) \\ \left\langle \boldsymbol{f}^{INT,u,e} \right\rangle &= \int_{\mathcal{B}^e} (\boldsymbol{B}^{u,e})^T \cdot \langle \boldsymbol{\sigma} \rangle \, dv \\ \widetilde{\boldsymbol{F}}^{INT,\breve{\varphi}} &= \mathop{\mathsf{A}}_{e \in \tilde{\mathcal{B}}^h} \left(\hat{q} \left\langle \boldsymbol{f}^{INT,\varphi,e} \right\rangle + \tilde{q}^e \boldsymbol{f}^{INT,\varphi,e} \right) \\ \widehat{\boldsymbol{F}}^{INT,\widehat{D}} &= \hat{q} \begin{bmatrix} \widehat{\boldsymbol{F}}^{INT,\hat{u}} \\ \widehat{\boldsymbol{F}}^{INT,\hat{\varphi}} \end{bmatrix} \\ \widehat{\boldsymbol{F}}^{INT,\hat{u}} &= \mathop{\mathsf{A}}_{e \in \hat{\mathcal{B}}^h} \left\langle \boldsymbol{f}^{INT,u,e} \right\rangle \ , \ \widehat{\boldsymbol{F}}^{INT,\hat{\varphi}} = \mathop{\mathsf{A}}_{e \in \hat{\mathcal{B}}^h} \left\langle \boldsymbol{f}^{INT,\varphi,e} \right\rangle \end{aligned} \tag{119}$$

where $\widetilde{\boldsymbol{F}}^{INT,D}$ is the internal force and moment vector associated with free nodal dofs in $\tilde{\mathcal{B}}^h$, $\widetilde{\boldsymbol{F}}^{INT,\widehat{D}}$ the internal force and moment vector associated with prescribed nodal dofs in $\tilde{\mathcal{B}}^h$, where $\widetilde{\boldsymbol{F}}^{INT,D}$ and $\widetilde{\boldsymbol{F}}^{INT,\widehat{D}}$ are extracted from the full internal force and moment vector $\widetilde{\boldsymbol{F}}^{INT,\breve{D}}$, with superscript $(\bullet)^{\breve{D}}$ denoting the full internal force and moment vector associated with elements in $\tilde{\mathcal{B}}^h$, $\tilde{q}^e$ is the partitioning coefficient of continuum potential energy associated with element $\mathcal{B}^e \subset \tilde{\mathcal{B}}^h$, and $\langle \bullet \rangle$ is a homogenization operator (to be defined later). A simple choice is a volume fraction $\tilde{q}^e = \tilde{r}^e$. (*13*) considered a more sophisticated approach using an atomic bond density function solved to reproduce a minimum potential energy state for homogeneous deformation. The analogy here for particles would be a particle contact density for the potential energy terms (internal force vectors). This will be considered further in future work. For now, we consider a

volume fraction partitioning through $\tilde{q}^e$, and a simple scaling through coefficients $\bar{q}$ (see 1D numerical examples). $\widehat{\boldsymbol{F}}^{INT,\widehat{D}}$ is the homogenized internal force vector associated with prescribed nodal dofs in $\hat{\mathcal{B}}^h$, which has no contribution if $\hat{q} = 0$, i.e., underlying particle contact forces and moments provide full contribution in $\hat{\mathcal{B}}^h$. $\bar{\boldsymbol{F}}^{INT,D}$ is the internal force vector associated with free nodal dofs in the pure continuum domain $\bar{\mathcal{B}}^h$. The external force and moment vectors are written as

$$
\begin{aligned}
\boldsymbol{F}^{EXT,D} &= \widetilde{\boldsymbol{F}}^{EXT,D} + \bar{\boldsymbol{F}}^{EXT,D} \\
\bar{\boldsymbol{F}}^{EXT,D} &= \left[\begin{array}{c} \bar{\boldsymbol{F}}^{EXT,u} \\ \bar{\boldsymbol{F}}^{EXT,\varphi} \end{array} \right] \\
\bar{\boldsymbol{F}}^{EXT,u} &= \boldsymbol{F}_t + \boldsymbol{F}_g^u + \mathop{\mathsf{A}}_{e \in \bar{\mathcal{B}}^h} \boldsymbol{f}_b^{EXT,u,e} \\
\bar{\boldsymbol{F}}^{EXT,\varphi} &= \boldsymbol{F}_r + \boldsymbol{F}_g^{\varphi} + \mathop{\mathsf{A}}_{e \in \bar{\mathcal{B}}^h} \boldsymbol{f}_\ell^{EXT,\varphi,e}
\end{aligned}
\tag{120}
$$

and

$$
\begin{aligned}
\boldsymbol{F}^{EXT,\widehat{D}} &= \widetilde{\boldsymbol{F}}^{EXT,\widehat{D}} + \widehat{\boldsymbol{F}}^{EXT,\widehat{D}} \\
\widetilde{\boldsymbol{F}}^{EXT,\breve{D}} &= \left[\begin{array}{c} \widetilde{\boldsymbol{F}}^{EXT,\breve{u}} \\ \widetilde{\boldsymbol{F}}^{EXT,\breve{\varphi}} \end{array} \right] \\
\widetilde{\boldsymbol{F}}^{EXT,\breve{u}} &= \mathop{\mathsf{A}}_{e \in \tilde{\mathcal{B}}^h} \left(\hat{q} \left\langle \boldsymbol{f}_b^{EXT,u,e} \right\rangle + \tilde{q}^e \boldsymbol{f}_b^{EXT,u,e} \right) \\
\widetilde{\boldsymbol{F}}^{EXT,\breve{\varphi}} &= \mathop{\mathsf{A}}_{e \in \tilde{\mathcal{B}}^h} \left(\hat{q} \left\langle \boldsymbol{f}_\ell^{EXT,\varphi,e} \right\rangle + \tilde{q}^e \boldsymbol{f}_\ell^{EXT,\varphi,e} \right) \\
\widehat{\boldsymbol{F}}^{EXT,\widehat{D}} &= \hat{q} \left[\begin{array}{c} \widehat{\boldsymbol{F}}^{EXT,\hat{u}} \\ \widehat{\boldsymbol{F}}^{EXT,\hat{\varphi}} \end{array} \right] \\
\widehat{\boldsymbol{F}}^{EXT,\hat{u}} &= \mathop{\mathsf{A}}_{e \in \hat{\mathcal{B}}^h} \left\langle \boldsymbol{f}_b^{EXT,u,e} \right\rangle \ , \ \widehat{\boldsymbol{F}}^{EXT,\hat{\varphi}} = \mathop{\mathsf{A}}_{e \in \hat{\mathcal{B}}^h} \left\langle \boldsymbol{f}_\ell^{EXT,\varphi,e} \right\rangle
\end{aligned}
\tag{121}
$$

where $\widetilde{\boldsymbol{F}}^{EXT,D}$ is the external body force and couple vector associated with free nodal dofs in $\tilde{\mathcal{B}}^h$, $\widetilde{\boldsymbol{F}}^{EXT,\widehat{D}}$ the external body force and couple vector associated with prescribed nodal dofs in $\tilde{\mathcal{B}}^h$, where $\widetilde{\boldsymbol{F}}^{EXT,D}$ and $\widetilde{\boldsymbol{F}}^{EXT,\widehat{D}}$ are extracted from $\widetilde{\boldsymbol{F}}^{EXT,\breve{D}}$, the total external body force and couple vector calculated in $\tilde{\mathcal{B}}^h$. $\widehat{\boldsymbol{F}}^{EXT,\widehat{D}}$ is the homogenized external body force and couple vector associated with prescribed nodal dofs in $\hat{\mathcal{B}}^h$, which has no contribution if $\hat{q} = 0$, i.e., underlying particle body forces and couples provide full contribution in $\hat{\mathcal{B}}^h$. $\bar{\boldsymbol{F}}^{EXT,D}$ is the external force and couple vector associated with free nodal dofs in the pure continuum FE domain $\bar{\mathcal{B}}^h$.

2.4.3 1D Full Overlap Coupling

Starting with equation 108, and referring to figure 7, we are able to arrive at a simplified set of nonlinear equations to solve for a fully overlapped particle-continuum region.

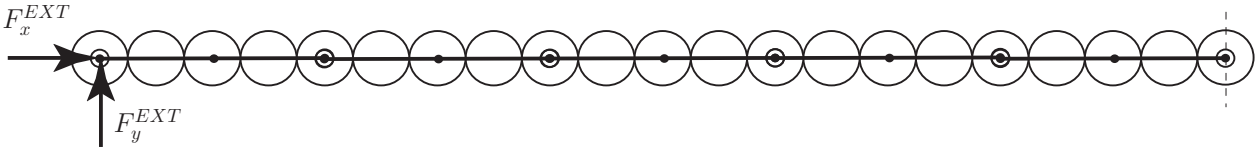

Figure 7. Domain of full overlap coupling between a 1-D string of twenty-one glued, Hertzian nonlinear elastic, spherical DEs, and a five-element 1-D micropolar linear elastic mesh.

We express the free dofs of a particle α in terms of the prescribed nodal dofs of an element e, such that

$$
\begin{aligned}
q_x^\alpha &= \boldsymbol{N}^{u,e}[\xi(x^\alpha)]\hat{\boldsymbol{d}}_x^e \\
q_y^\alpha &= \boldsymbol{N}^{v,e}[\xi(x^\alpha)]\hat{\boldsymbol{d}}_y^e \\
\omega^\alpha &= \boldsymbol{N}^{\theta,e}[\xi(x^\alpha)]\hat{\boldsymbol{d}}_\theta^e \\
\boldsymbol{q}^\alpha &= \boldsymbol{N}^\alpha_{Q\hat{D}}\hat{\boldsymbol{d}}^e \ , \quad \boldsymbol{N}^\alpha_{Q\hat{D}} = \begin{bmatrix} N_1^u & 0 & 0 & 0 & N_2^u & 0 & 0 \\ 0 & N_1^v & 0 & N_3^v & 0 & N_2^v & 0 \\ 0 & 0 & N_1^\theta & 0 & 0 & 0 & N_2^\theta \end{bmatrix} \\
\boldsymbol{N}_{Q\hat{D}} &= \mathop{\mathsf{A}}_{\alpha=1}^{n_{\text{particles}}} \boldsymbol{N}^\alpha_{Q\hat{D}} \\
\boldsymbol{M}_{\hat{D}\hat{D}} &= \boldsymbol{N}^T_{Q\hat{D}}\boldsymbol{N}_{Q\hat{D}} \\
\boldsymbol{B}_{\hat{D}Q} &= \boldsymbol{M}^{-1}_{\hat{D}\hat{D}}\boldsymbol{N}^T_{Q\hat{D}}
\end{aligned}
$$

where $\xi(x^\alpha) = (2/h^e)[x^\alpha - (x_1^e + x_2^e)/2]$, and the resulting nonlinear equations to solve for $\boldsymbol{Q}$, with $\hat{\boldsymbol{D}} = \boldsymbol{B}_{\hat{D}Q}\boldsymbol{Q}$ and $\boldsymbol{F}^{INT,\hat{D}}(\hat{\boldsymbol{D}}) = \boldsymbol{K}^D(\boldsymbol{B}_{\hat{D}Q}\boldsymbol{Q})$, are

$$
(1-\hat{q})\boldsymbol{F}^{INT,Q}(\boldsymbol{Q}) + \hat{q}\boldsymbol{B}^T_{\hat{D}Q}\boldsymbol{K}^D(\boldsymbol{B}_{\hat{D}Q}\boldsymbol{Q}) = \boldsymbol{F}^{EXT,Q} \tag{122}
$$

The twenty-one 1-cm diameter DE spheres, and overlaying five-element micropolar elastic mesh in figure 7 are used to demonstrate the overlap coupling procedure. The parameters are modified slightly from the Timoshenko beam convergence example: $F_x^{EXT} = 10$kN, $F_y^{EXT} = 10$kN, $E = 29$GPa, $\nu = 0.25$, $\kappa = 0.1\mu$, and $\gamma = 400\ell^2\mu$, $\ell = 1$cm, $R = 5$mm, $B = 50$, $\bar{q}^u = 0.077$, $\bar{q}^v = 5.5$, $\bar{q}^\theta = 1.0$. *Notice the micropolar couple modulus* γ *is* $\approx 3 * 400/0.05 = 24,000$ *times*

larger than used for the results reported in figure 4. See more discussion later. The different $\bar{q}$'s indicate which equation they influence in the scaling of micropolar elastic FE stiffness (u for axial, v for transverse, and θ for rotation). The axial load F_x^{EXT} is first applied to DE particle 1 (same $x = 0$ position as node 1 of FE mesh) to generate a transverse stiffness from the Hertz-Mindlin nonlinear theory, and then the transverse loading F_y^{EXT} is applied while the axial load is held fixed. The end moment at $x = 0$ is zero. It is cantilevered at $x = L$ (zero axial and transverse displacement, and zero rotation). The results in figure 8 demonstrate how the DE and FE results can be nearly matched by scaling the micropolar elastic stiffness with the $\bar{q}$'s. The rotations of the FE and DE do not match closely, and there is no coupling between DE and FE. This example demonstrates the scaling through $\bar{q}$ of the micropolar elastic FE stiffness. Also, because of the relatively stiff transverse response of the nonlinear Hertzian DE spheres in contact after 1-cm of compression (this is a large strain compression for a Hertzian theory, which is valid only for small strains, but we use it to demonstrate the overlap coupling), the value of the micropolar couple modulus γ was increased by a factor of $\approx 3 * 400/0.05 = 24,000$, thus the large transverse displacement observed in figure 4 versus figure 8. We keep the parameters of the Hertzian elastic contact model constant, and vary the micropolar elastic model parameters to match the Hertzian model. This micropolar elastic parameter variation and energy scaling through the $\bar{q}$'s take the place, for now, of the homogenization operator $\langle \bullet \rangle$ discussed in the previous section on the overlap coupling method. This will be revisited in future work. Also, in figure 8 we use 10 times the axial and transverse end forces F_x^{EXT} and F_y^{EXT} when compared to figure 4.

Using the same micropolar stiffness scaling coefficients $\bar{q}$'s, and equation 122, and with energy factor coefficients $\hat{q}^u = 0.65$, $\hat{q}^v = 0.5$, $\hat{q}^\theta = 0.5$, we get the results in figure 9. Notice that the energy is factored between the DE particles and FE micropolar mesh. The DE particle rotations oscillate about the FE nodal rotations. Notice that the *particle 1* axial force ≈ 6.3kN and the *particle 1 projected from rod node 1* axial force ≈ 3.6kN add up to the $F_x^{EXT} = 10$kN through equation 122. Likewise for the transverse force. This is the effect of the energy factor coefficients $\hat{q}$'s, whereas energy partitioning coefficient $\tilde{q}$ has no effect because there is no partial overlap region (i.e., $\tilde{\mathcal{B}}^h = \emptyset$), only a full overlap region $\hat{\mathcal{B}}^h$ (see figure 6).

If we set the energy factor coefficients $\hat{q}^u = 0$, $\hat{q}^v = 0$, $\hat{q}^\theta = 0$, we get the results in figure 10. Notice that the micropolar FE mesh contributes no energy to the system. The particle DE simulation provides all the energy, and in the rotations, they oscillate.

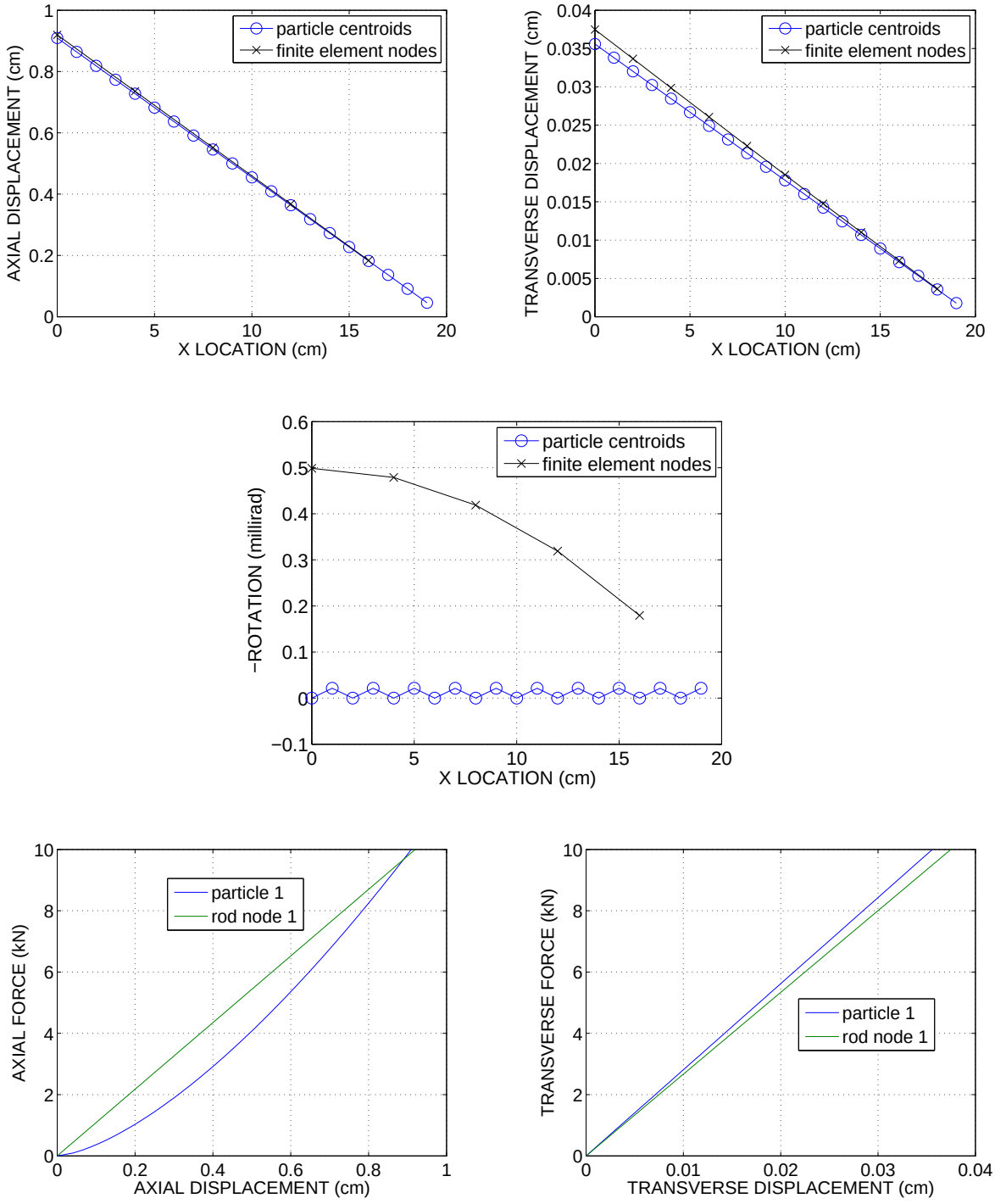

Figure 8. Full overlap results with scaling coefficients $\bar{q}$'s on micropolar stiffness, but no coupling.

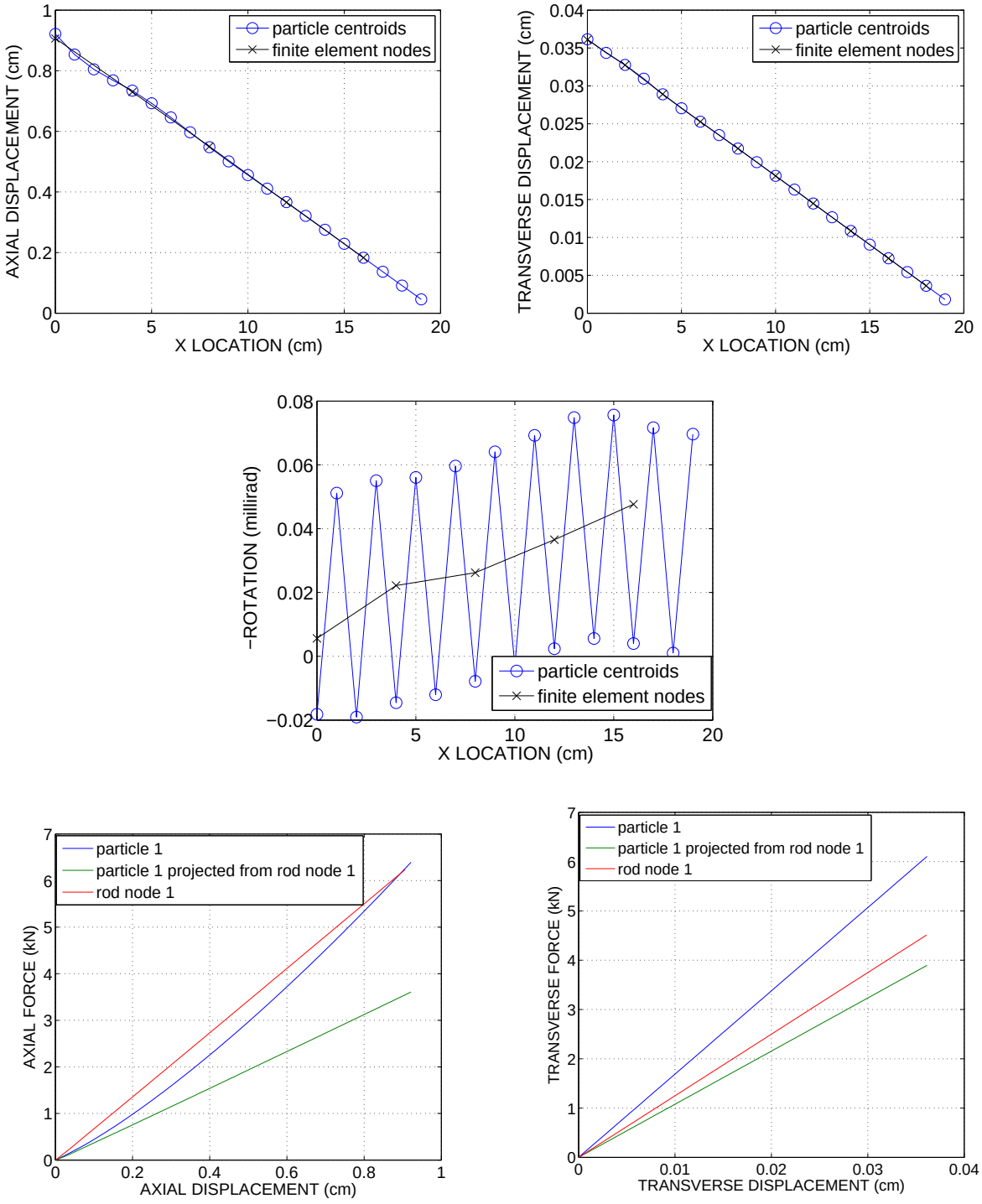

Figure 9. Full overlap coupling results with energy factor coefficients $\hat{q}^u = 0.65$, $\hat{q}^v = 0.5$, $\hat{q}^\theta = 0.5$.

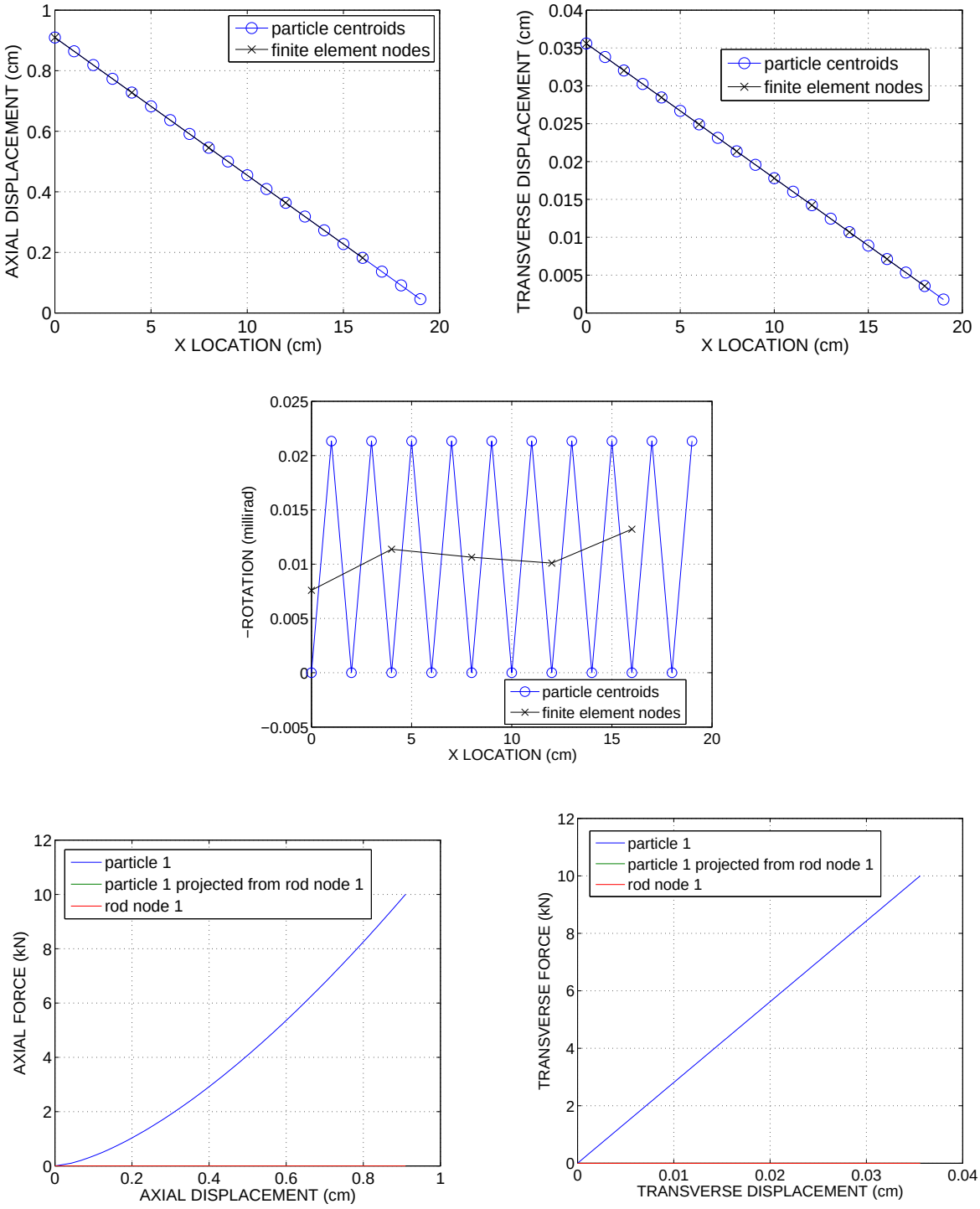

Figure 10. Full overlap coupling results with energy factor coefficients $\hat{q}^u = 0$, $\hat{q}^v = 0$, $\hat{q}^\theta = 0$.

2.4.4 1D Partial Overlap Coupling with Partial Overlay 1D Micropolar FE

Referring to figure 11, $\boldsymbol{N}_{QD} = \boldsymbol{0}$ because there is no overlap between free particle dofs and free continuum dofs. We need the additional interpolation matrices for particle α

$$\boldsymbol{N}^{\alpha}_{\hat{Q}\hat{D}} = \begin{bmatrix} 0 & 0 & 0 & 0 & N^u_1 & 0 & 0 \\ 0 & 0 & 0 & 0 & 0 & N^v_1 & 0 \\ 0 & 0 & 0 & 0 & 0 & 0 & N^\theta_1 \end{bmatrix} \tag{123}$$

$$\boldsymbol{N}^{\alpha}_{\hat{Q}D} = \begin{bmatrix} 0 & N^u_2 & 0 & 0 \\ N^v_3 & 0 & N^v_2 & 0 \\ 0 & 0 & 0 & N^\theta_2 \end{bmatrix} \tag{124}$$

where we can then relate prescribed dof to free dof through the projection operators as

$$\begin{aligned} \boldsymbol{N}_{Q\hat{D}} &= \mathop{\mathbf{A}}_{\alpha=1}^{n_{\text{particles}}} \boldsymbol{N}^{\alpha}_{Q\hat{D}} \\ \boldsymbol{N}_{\hat{Q}\hat{D}} &= \mathop{\mathbf{A}}_{\alpha=1}^{n_{\text{particles}}} \boldsymbol{N}^{\alpha}_{\hat{Q}\hat{D}} \\ \boldsymbol{N}_{\hat{Q}D} &= \mathop{\mathbf{A}}_{\alpha=1}^{n_{\text{particles}}} \boldsymbol{N}^{\alpha}_{\hat{Q}D} \\ \boldsymbol{M}_{\hat{D}\hat{D}} &= \boldsymbol{N}^T_{Q\hat{D}} \boldsymbol{N}_{Q\hat{D}} \ , \ \boldsymbol{B}_{\hat{D}Q} = \boldsymbol{M}^{-1}_{\hat{D}\hat{D}} \boldsymbol{N}^T_{Q\hat{D}} \\ \boldsymbol{B}_{\hat{Q}Q} &= \boldsymbol{N}_{\hat{Q}\hat{D}} \boldsymbol{B}_{\hat{D}Q} \\ \boldsymbol{B}_{\hat{Q}D} &= \boldsymbol{N}_{\hat{Q}D} \end{aligned}$$

$$\begin{aligned} \hat{\boldsymbol{Q}} &= \boldsymbol{B}_{\hat{Q}Q} \boldsymbol{Q} + \boldsymbol{B}_{\hat{Q}D} \boldsymbol{D} \\ \hat{\boldsymbol{D}} &= \boldsymbol{B}_{\hat{D}Q} \boldsymbol{Q} \end{aligned}$$

where we solve the coupled system of nonlinear balance equations as (simplified from equations 108 and 109)

$$\boldsymbol{R}^Q(\boldsymbol{Q}, \boldsymbol{D}) = \boldsymbol{F}^{INT,Q}(\boldsymbol{Q}) + \boldsymbol{B}^T_{\widehat{Q}Q} \boldsymbol{F}^{INT,\widehat{Q}}(\widehat{\boldsymbol{Q}}) + \boldsymbol{B}^T_{\widehat{D}Q} \boldsymbol{F}^{INT,\widehat{D}}(\widehat{\boldsymbol{D}}) - \boldsymbol{F}^{EXT,Q} = \boldsymbol{0} \tag{125}$$

$$\boldsymbol{R}^D(\boldsymbol{Q}, \boldsymbol{D}) = \boldsymbol{B}^T_{\widehat{Q}D} \boldsymbol{F}^{INT,\widehat{Q}}(\widehat{\boldsymbol{Q}}) + \boldsymbol{F}^{INT,D}(\boldsymbol{D}) - \boldsymbol{F}^{EXT,D} = \boldsymbol{0} \tag{126}$$

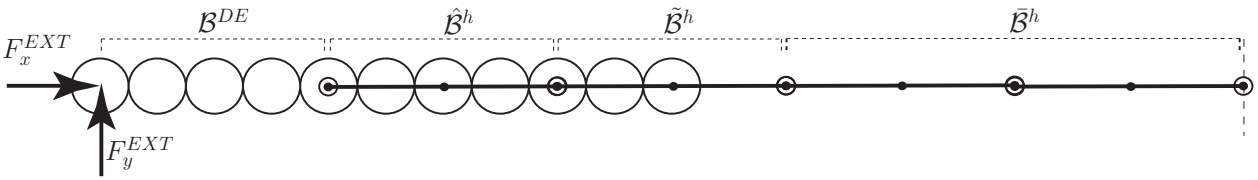

Figure 11. Domain of partial overlap coupling between a 1D string of 11 glued, Hertzian nonlinear elastic, spherical DEs, and a 4 element 1D micropolar linear elastic mesh.

For volume average energy partitioning in the overlap region $\tilde{\mathcal{B}}^h$, $\tilde{q} = (h^e A^e - 2.5(4/3)\pi R^3)/(h^e A^e) = 0.583$ because there are 2.5 particle volumes in $\tilde{\mathcal{B}}^h$. We illustrate the performance of the overlap coupling algorithm in figures 12 and 13. We can see that with scaling of micropolar elasticity through the $\bar{q}$ coefficients, we can achieve a homogeneous axial displacement gradient across the overlap coupling region $\tilde{\mathcal{B}}^h$, whereas the transverse component cannot be made homogeneous. This can be observed because of the ratcheting of the DE particle rotations, which the micropolar continuum FE can only represent if the element length h^e is chosen to be one DE particle diameter, which defeats the purpose of the overall overlap coupling strategy. We believe that with more particles in 2D and 3D, as illustrated in figure 6, the particle displacements and rotations will be smoothed and, thus, the overlap coupling should work more effectively. In a sense, this 1D example assumes "too discrete" a 1D DE particle string, that exhibits an oscillation/ratcheting behavior upon transverse shear loading. The axial component is handled without trouble.

We set the micropolar scaling coefficients $\bar{q}^u = 0.0195$, $\bar{q}^v = 0.8$, $\bar{q}^\theta = 0.85$ in $\mathcal{B}^h = \hat{\mathcal{B}}^h \cup \tilde{\mathcal{B}}^h \cup \bar{\mathcal{B}}^h$ for 1D micropolar FE stiffness; energy factor coefficients $\hat{q}^u = 0$, $\hat{q}^v = 0$, $\hat{q}^\theta = 0$ in $\hat{\mathcal{B}}^h \cup \tilde{\mathcal{B}}^h$; and energy partitioning coefficient $\tilde{q} = 0.583$ in $\tilde{\mathcal{B}}^h$. The "not scaled" plots indicate that $\bar{q}^u = 1$, $\bar{q}^v = 1$, $\bar{q}^\theta = 1$. The results are shown in figure 12.

If we set the micropolar scaling coefficients the same $\bar{q}^u = 0.0195$, $\bar{q}^v = 0.8$, $\bar{q}^\theta = 0.85$, and energy factor coefficients $\hat{q}^u = 0$, $\hat{q}^v = 0$, $\hat{q}^\theta = 0.9$, then we have the result in figure 13. Notice how factoring some of the DE rotational energy to the 1D micropolar FE mesh reduces the oscillations of the DE particles in the transition/overlap region.

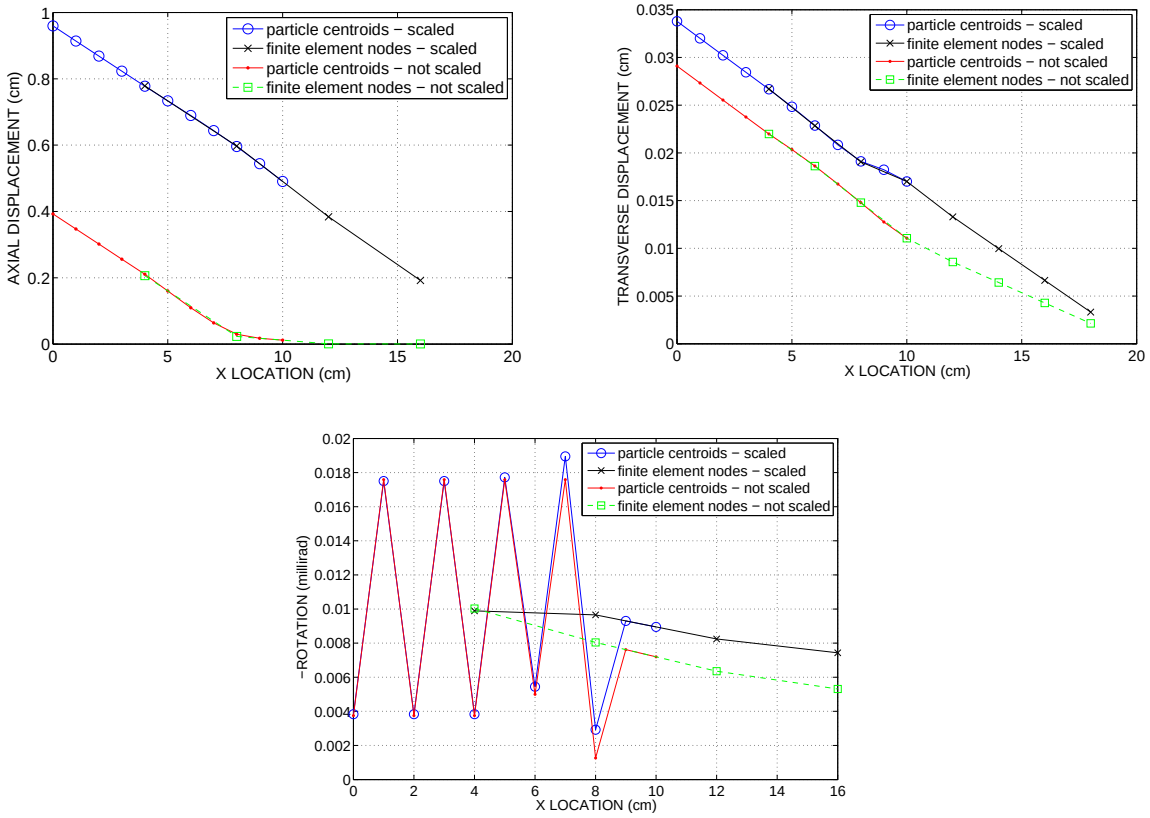

Figure 12. Partial overlap coupling results for energy factor coefficients $\hat{q}^u = 0$, $\hat{q}^v = 0$, $\hat{q}^\theta = 0$.

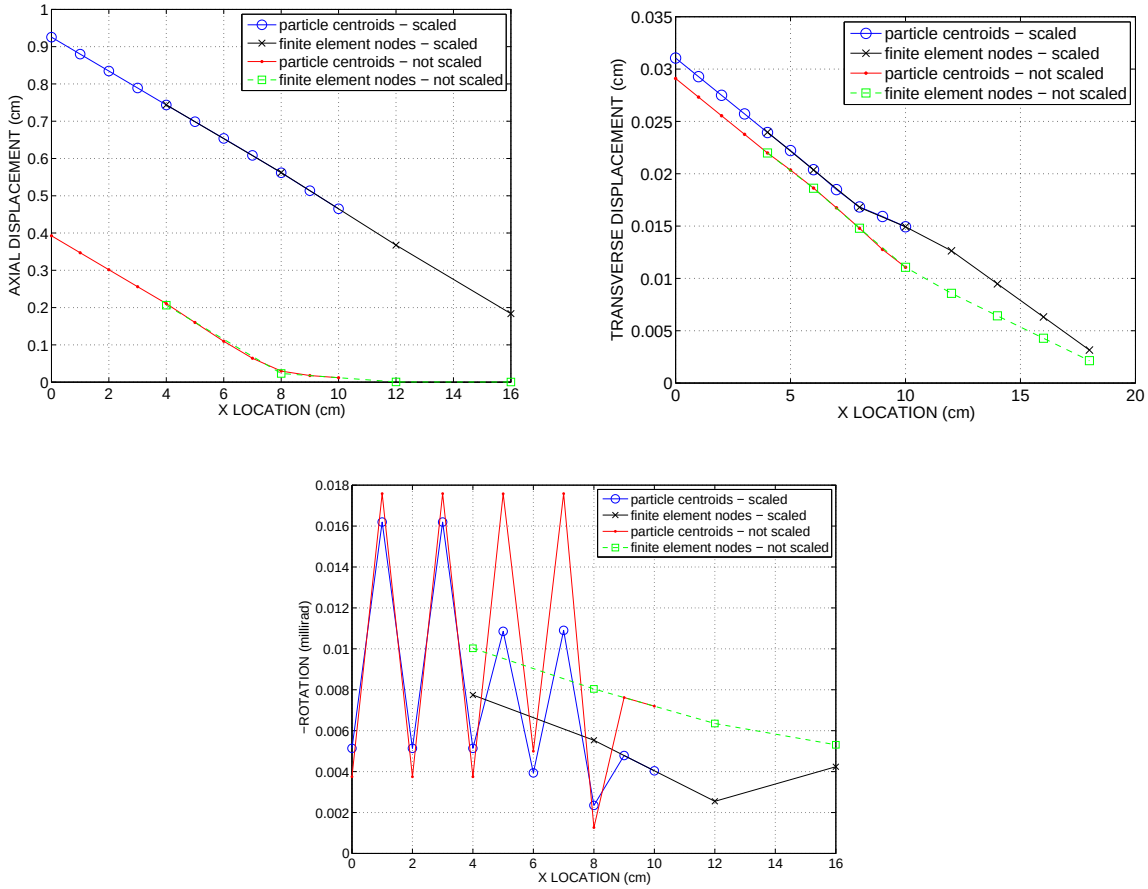

Figure 13. Partial overlap coupling results for energy factor coefficients $\hat{q}^u = 0$, $\hat{q}^v = 0$, $\hat{q}^\theta = 0.9$.

3. Summary

3.1 Results

The details of a 1-D overlap coupling between a micropolar linear isotropic elastic finite element (FE) model and a 1D string of Hertzian (nonlinear) elastic-at-contact discrete element (DE) spheres were presented. Numerical examples demonstrated various overlapping domains: (1) full overlap coupling with fully-informed upscaled micropolar FE response from the underlying DE response, and (2) partial overlap coupling with partially-informed upscaled micropolar FE response (along partial length of domain) from the underlying DE response (also along partial length of domain).

3.2 Conclusions

The simple 1D problem presented in this report provides an accessible model problem through which to better understand how such coupling strategies should work for overlap coupling of underlying DNS particulate models (in this case, DE), and overlying generalized continuum models (in this case, micropolar elasticity). What makes this coupling strategy different than those for atomistic continuum coupling methods (*13, 19*) is the rotational degrees of freedom of the DE model, the open window $\mathcal{B}^{DE}$ region, and the additional degrees of freedom inherent in the generalized continuum models—in this case a micropolar continuum (a subset of micromorphic continuum).

3.3 Future Work

Future work will first involve extending the 1D formulation and implementation to include inertia terms to study wave propagation (axial, transverse, and rotational) along the 1D domain. Extending these concepts for the envisioned full 3D overlap coupling problem and micromorphic continuum as outlined in section 1.1 will come next.

4. References

1. Chawla, N.; Ganesh, V.; Wunsch, B. Three-dimensional (3D) microstructure visualization and finite element modeling of the mechanical behavior of SiC particle reinforced aluminum composites. *Scripta Mater.* **2004**, *51* (2), 161–165.

2. Baer, M.; Hall, C.; Gustavsen, R.; Hooks, D.; Sheffield, S. Isentropic loading experiments of a plastic bonded explosive and constituents. *J. Appl. Phys.* **2007**, *101* (3), 34906-1–12.

3. Hughes, T. J. R. *The Finite Element Method*; Prentice-Hall: New Jersey: 1987.

4. Chen, W.; Ravichandran, G. Dynamic compressive failure of a glass ceramic under lateral confinement. *J. Mech. Phys. Solids* **1997**, *45*, 1303–28.

5. Caballero, A.; Carol, I.; Lopez, C. A meso-level approach to the 3D numerical analysis of cracking and fracture of concrete materials. *Fatigue Fract. Eng. Mater. Struct.* **2006**, *29* (12), 979–991.

6. Kraft, R.; Molinari, J.; Ramesh, K.; Warner, D. Computational micromechanics of dynamic compressive loading of a brittle polycrystalline material using a distribution of grain boundary properties. *J. Mech. Phys. Solids* **2008**, *56*, 2618–41.

7. Kraft, R.; Molinari, J. A statistical investigation of the effects of grain boundary properties on transgranular fracture. *Acta Mater.* **2008**, *56* (17), 4739–49.

8. Vogler, T.; Clayton, J. Heterogeneous deformation and spall of an extruded tungsten alloy: plate impact experiments and crystal plasticity modeling. *J. Mech. Phys. Solids* **2008**, *56* (2), 297–335.

9. Regueiro, R. On finite strain micromorphic elastoplasticity. *Int. J. Solids Struct.* **2010**, *47*, 786–800.

10. Isbuga, V.; Regueiro, R. Three-dimensional finite element analysis of finite strain micromorphic linear isotropic elasticity. *International Journal of Engineering Science* **2011**, *49*, 1326–1336.

11. Hertz, H. Ueber die Berührung fester elastischer Körper. [On the fixed elastic body contact]. *Journal für die reine und angewandte Mathematik (Crelle)* **1882**, *92*, 156–171.

12. Mindlin, R. Compliance of elastic bodies in contact. *J. App. Mech.* **1949**, *16* (3), 259–268.

13. Klein, P.; Zimmerman, J. Coupled atomistic-continuum simulations using arbitrary overlapping domains. *J. Comput. Phys.* **2006**, *213* (1), 86–116.

14. Eringen, A. *Nonlinear Theory of Continuous Media*; 1 ed.; McGraw-Hill: 1962.

15. Eringen, A. Theory of Micropolar Elasticity. In *Fracture, An Advanced Treatise*; Vol. 2; Liebowitz, H., Ed.; Academic Press: 1968.

16. Pinsky, P. unpublished course notes, Stanford University . 2001.

17. Eringen, A. *Microcontinuum Field Theories I: Foundations and Solids*; Springer-Verlag: 1999.

18. Yan, B.; Regueiro, R.; Sture, S. Three dimensional discrete element modeling of granular materials and its coupling with finite element facets. *Eng. Comput.* **2010**, *27* (4), 519–550.

19. Wagner, G.; Liu, W. Coupling of atomistic and continuum simulations using a bridging scale decomposition. *J. Comput. Phys.* **2003**, *190* (1), 249–74.

20. Rayleigh, J. *The Theory of Sound. Volume 1*; 1 ed.; Dover Pub. Inc., New York: 1945.

NO. OF
COPIES ORGANIZATION

1 Administrator
Defense Technical Info Center
Attn: DTIC OCP
8725 John J Kingman Rd Ste 0944
Ft. Belvoir, VA 22060-6218

1 U.S. Army Research Laboratory
IMHE ALC HRR Mail and Records Mgmt
RDRL CIO LL Technical Library

3 U.S. Army Research Laboratory
Dr. John Clayton
RDRL-WMP-B
Aberdeen Proving Ground, MD
21005-5066

5 University of Colorado, Boulder
Prof. Richard Regueiro
1111 Engineering Dr.
428 UCB, ECOT 441
Boulder, CO 80309-0428

12 U.S. Army Research Laboratory
R. Becker [1]
S. Bilyk [1]
D. Dandekar [1]
M. Greenfield [1]
C. Hoppel [1]
B. Leavy [1]
B. Love [1]
Y. Huang [1]
R. Kraft [1]
M. Raftenberg [1]
M. Scheidler [1]
C. Williams [1]
RDRL-WMP-B
Aberdeen Proving Ground, MD
21005-5066

1 U.S. Army Research Laboratory
Dr. Todd Bjerke
RDRL-WMP-C
Aberdeen Proving Ground, MD
21005-5066

1 U.S. Army Research Laboratory
Dr. Neil Gniazdowski
RDRL-WMP-F
Aberdeen Proving Ground, MD
21005-5066

INTENTIONALLY LEFT BLANK.